DISS. Nr. 6224

K_L TOTAL CROSS-SECTION AND K_S COHERENT REGENERATION ON NUCLEI

BETWEEN 30 AND 130 GeV/c

A Dissertation submitted

to the

SWISS FEDERAL INSTITUTE OF TECHNOLOGY

ZURICH

for the degree of

Doctor of Natural Sciences

Presented by

ANDRE GSPONER

graduate in physics of the University of Lausanne

born March 29, 1948

from Ausserberg (VS)

Accepted on the recommendation of

Prof. V.L. Telegdi, Referee

Prof. H. Hofer, Co-Referee

1978

SECTION EFFICACE TOTALE DE K_L ET REGENERATION COHERENTE DE K_S

SUR NOYAUX ENTRE 30 ET 130 GeV/c

ABSTRACT

Des mesures à haute statistique des sections efficaces totales ($\pm 1.5\%$) et de la regeneration coherente ($\pm 3\%$) sur C, Al, Cu, Sn et Pb permettent de tester en détail la phenomenologie de Glauber-Regge à haute energie.

Les états inélastiques intermédiaires, dont la contribution dans le Pb est de l'ordre de 10% à 100 GeV/c, sont correctement prédit par un modèle de Karmanov-Kondratyuk amélioré. Les résultats peuvent être interprétés avec des rayons quadratiques moyens nucléaires égaux aux rayons électromagnétiques correspondants. La prédiction du modèle pour la section efficace totale des K_L est directement compatible avec les données, alors que la prédiction de la régéneration cohérente sur noyaux nécessite un intercepte de la trajectoire de l'ω, $\alpha_\omega(0)=0.40\pm0.01$, nettement différent du même intercept, $\alpha_\omega(0)=0.44\pm0.01$, mesuré sur cibles élémentaires.

A Louis Dick

K_L TOTAL CROSS-SECTION AND K_S COHERENT REGENERATION ON NUCLEI

BETWEEN 30 AND 130 GeV/c

ABSTRACT

High-statistics measurements of total cross-section ($\pm 1.5\%$) and coherent regeneration ($\pm 3\%$) on C, Al, Cu, Sn and Pb, allow the Glauber-Regge phenomenology to be extensively tested at high energies. The inelastic intermediate states, which contribute as much as 10% in Pb at 100 GeV/c, are properly accounted for by an improved Karmanov and Kondratyuk model. The data can be interpreted with nuclear strong interaction RMS radii equal to the corresponding electromagnetic radii. The model prediction for the K_L total cross-section is directly compatible with the data, while the prediction of K_S regeneration on nuclei requires an ω intercept $\alpha_\omega(0)=0.40\pm 0.01$ significantly different from the same intercept $\alpha_\omega(0)=0.44\pm 0.01$ measured with elementary particle targets.

TABLE OF CONTENTS

1.   INTRODUCTION AND MOTIVATION.

1.1. Neutral kaons.

They are many interesting effects associated with the existence of two neutral kaons, which are distinguished by their strangeness:

$$S|K^o\rangle = +|K^o\rangle$$
$$S|\bar{K}^o\rangle = -|\bar{K}^o\rangle \tag{1.1}$$

Among them, the existence of two states with distinct lifetimes and the CP violation phenomenon are the most important[1].

Since CP is known to be conserved by the weak interactions in general, one expects the decay eigenstates to be

$$\sqrt{2}\,|K_1\rangle = |K^o\rangle + |\bar{K}^o\rangle$$
$$\sqrt{2}\,|K_2\rangle = |K^o\rangle - |\bar{K}^o\rangle \tag{1.2}$$

such that

$$CP|K_1\rangle = +|K_1\rangle$$
$$CP|K_2\rangle = -|K_2\rangle \tag{1.3}$$

But, in the K^o-$\bar{K}^o$ system, CP has been found to be violated, although at the 10^{-3} level only. The true decay states are thus

$$\sqrt{1+|\varepsilon|^2}\,|K_S\rangle = |K_1\rangle + \varepsilon|K_2\rangle$$
$$\sqrt{1+|\varepsilon|^2}\,|K_L\rangle = |K_2\rangle + \varepsilon|K_1\rangle \tag{1.4}$$

In the superweak theory of CP violation, the complex parameter ε is equal to η_{+-}, where

$$\eta_{+-} \equiv \frac{\langle \pi^+\pi^- | K_L \rangle}{\langle \pi^+\pi^- | K_S \rangle} \tag{1.5}$$

In this experiment we shall exploit the fact that in a K_L beam, there is an <u>almost equal mixture of particles</u> (K^O) and <u>anti-particles</u> ($\bar{K}^O$). Indeed, from (1.2) and (1.4)

$$\sqrt{2\left(1 + |\varepsilon|^2\right)} \; |K_L\rangle = \left(1+\varepsilon\right)|K^O\rangle - \left(1-\varepsilon\right)|\bar{K}^O\rangle \tag{1.6}$$

and K_L's are thus idealy suited for comparing particle and anti-particle properties.

Two kind of processes are readily accessible :

(i) K_L <u>total cross-section</u> measurement, i.e. the process

$$K_L + A \longrightarrow K_L + A$$
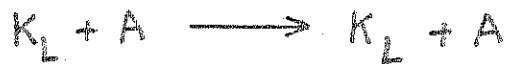
which is directly proportional to the <u>sum</u> of the K^O, $\bar{K}^O$ scattering amplitudes at $t=0$:

$$\sigma_T = \frac{4\pi}{P} \; \text{Im} \; \frac{f(o) + \bar{f}(o)}{2} \tag{1.7}$$

(ii) K_S <u>coherent regeneration</u> measurement, i.e. the process

$$K_L + A \longrightarrow K_S + A$$

which is directly proportional to the <u>difference</u> of the K^O, $\bar{K}^O$ scattering amplitudes at $t=0$:

$$\tilde{\rho} = \left| \frac{f(o) - \bar{f}(o)}{P} \right| \tag{1.8}$$

We shall now examine in details the motivation for studying these two processes with high accuracy, and for several nuclear targets.

1.2. Total cross-section measurement

Total cross-sections of charged particles are difficult to measure because of Coulomb interference effects. Neutral particles of course do not suffer from this inconvenience, and thus allow very precise measurements to be performed easily. It is probably for this reason that total cross-sections on nuclear targets have been measured first for neutron beams at Fermilab energies[2]. In these later experiments, substantial departures from the standard Glauber model of hadron-nucleus interactions[3] have been observed, and interpreted to come from the so-called "inelastic screening" effect, i.e., from the contribution of inelastic intermediate states[4]. The present experiment with kaons will confirm this effect and study its atomic number dependence with an increased precision. Furthermore, since the kaon-nucleon total cross-section is smaller than the corresponding neutron-nucleon cross-section, the kaon mean free path inside the nucleus is larger, and the inelastic screening effects will hence be comparatively bigger for kaons than for neutrons. Finally, the kaons have the technical advantage over neutrons that they can be detected in vacuum (through their semi-leptonic decays), while the neutrons need a converter to be detected. Provided one properly takes care of the well-known rate effects in such an experiment, it becomes possible to devise a virtually systematic-free measurement of the K_L-nucleus total cross-sections.

1.3. Regeneration measurement

It is well known that a most powerful technique for the study of the difference in behavior between particle and anti-particle is that of coherent regeneration. The power of this technique results in part from the following:

a) The events rate for the process K_L + target $\longrightarrow$ K_S + target is directly proportional to the absolute square of the difference of the particle/anti-particle scattering amplitudes. Thus, as one measures this difference directly, an important source of systematics involved in substraction of two large numbers is eliminated.

b) Even through the yield of anti-particles (from the production target) falls rapidly with energy, one does not suffer: the weak interaction acts to convert the dominant K^O's (particles) into $\bar{K}^O$'s (anti-particles) so that the neutral K_L beam contain an (almost) equal mixture of particle/anti-particle.

In this experiment, we will exploit the effect of coherent regeneration, optimized to perform a high statistics study of the atomic number dependence of the difference between the K^O and $\bar{K}^O$ scattering amplitudes.

Apart from allowing a sensitive test of the Glauber model in the 30-130 GeV energy range, regeneration measurements have also the following attractive features:

(i)   The K^O, $\bar{K}^O$ amplitudes difference measured by K_S regeneration is keeping only the C = -1 Regge-poles contribution. This elimination of the diffractive term allows the poles, and thus the Regge theory, to be studied directly. In isoscalar targets (i.e. C), the ω-trajectory will be the dominant one left to be exchanged[5], while in I $\neq$ 0 targets (heavy nuclei or hydrogen) the ρ-trajectory will also contribute.

(ii) A systematic study of Regge phenomenology on nuclei should help understanding the discrepancy between the ω intercept measured on a I = 0 nucleus (i.e. carbon gives $\alpha_\omega(0)=0.40\pm0.01$ [5]) and the same intercept obtained by Regge fits to the elementary particles total cross-sections (i.e. $\alpha_\omega(0)=0.44\pm0.01$ [6]). For instance, in measurements on nuclei, a coupling with the pomeron may arise that can

modify the intercept[7]. The study of the atomic number dependence of regeneration could thus yield information on the relative importance of such "Regge cuts" contributions.

(iii) The full regeneration amplitude is equaly sensitive to the imaginary part _and_ the _real part_ of the K^O, $\overline{K}^O$ amplitude difference. In heavy nuclei, because of the rise of the total cross-sections, the Glauber model predicts a change in slope in the momentum dependence. In such effects the real parts of the kaon-nucleon amplitudes are essential.

(iv) The regeneration amplitude is known to be about 2.5 times larger on neutrons than on protons. Therefore, regeneration will be particularly sensitive to the _neutron distribution_ in heavy nuclei and will allow the comparison of proton and neutron density distributions[40].

(v) The _inelastic intermediate states_ will certainly contribute to the regeneration signal. As this process is not well known at present, it is of course interesting to observe it in regeneration as well. This phenomenon, which arises because of the rescattering of excited beam particles within the nucleus, yields information on the space--time development of strong interaction inside nuclear matter.

Together with the high-statistics, systematic-free measurements of the K_L total cross-sections themselves, as well as their momentum dependence, this experiment will study Al, Cu, Sn and Pb over the momentum range 30 to 130 GeV/c. Coupled with present data on H and C, this will provide measurements over a wide sweep in atomic number.

2.   EXPERIMENTAL METHOD

In order to significantly reduce systematic errors for this and subsequent experiments, the neutral beam-line was configurated so as to have two sharply separated beams of equal solid angle close to each other. Such a double beam arrangement allows one of the beams to be used for monitoring and the other one to contain the targets.

The major advantage of this technique comes from the fact that the same detection apparatus can be used simultaneously for both the monitoring - and the measurement. There is thus no independent beam monitor which in single beam experiments is a important source of systematics. As every accelerator pulse contains both the monitoring and the measured data, any intensity fluctuations in the beam or instabilities in the apparatus are of negligible consequence.

Of course, the roles of the two beams have to be interchanged every pulse by alternation of the target(s) between the beams. This insures that the result is insensitive to differences in fluxes in the two beams (i.e. arising from their slightly different production angles) and to any possible differences in the efficiency for the detection of decays from the beams.

2.1. Total cross-section measurement

With the double beam, the total cross-section $\sigma_T(K_L$, Nucleus) is measured by placing an absorber in one of the beams, far upstream of the decay region in which semi-leptonic decays from the two beams are detected (Fig. 2.1). Alternating the absorber between the two beams, one insures the equality of the incident fluxes of the two beams. If N_T is the number of transmitted and N_I the number of incident kaons (monitored in the other beam), the total cross-section in perfect geometry is readily given by

$$\sigma_T = \frac{A}{\rho L \mathcal{N}} \log\left(\frac{N_I}{N_T}\right) \qquad (2.1)$$

where A, ρ, L are respectively the atomic weight, density and length of the target, and $\mathcal{N}$ Avogadro's number.

The main advantage of this double beam technique comes of course from the fact that the same apparatus is used to measure N_T and N_I simultaneously. But, furthermore the average intensity through the detector is kept constant, i.e. the well-known "target-in", "target-out" rate corrections of single beam transmission experiments are absent.

Because of the length of the beam line required for the regeneration measurement, (see 2.2) it was possible to measure the total cross-section in "good geometry". With an absorber detector distance of 302 m and a beam spot size of 5.75 cm x 5.75 cm at the spectrometer, only two minor (a few percent) corrections with respect to (2.1) were needed, viz.

(1) Diffraction in the absorber

This correction is to take into account K_L's which diffract in the absorber and yet remain within the beam. This correction requires the knowledge of the solid angle $d\Omega$ defined by the collimators and the scattering parameters of the (K_L-nucleus) interaction. The latter parameters could be determined with sufficient precision from the model used to interpret the data.

Let us parametrize the differential elastic scattering on the nucleus as

$$\left(\frac{d\sigma}{d\Omega}\right)_{el} = \frac{p^2}{\pi} \frac{d\sigma}{dt} = \frac{p^2}{\pi} \sigma_T \, a \, b \, exp\left(-b|t|\right) \qquad (2.2)$$

Where a is the ratio of the elastic to the total (K_L-nucleus) cross-section. The probability of a K_L to scatter elastically n times in the

absorber is

$$P_S(n) = \frac{(ax)^n}{n!} \exp(-x) \tag{2.3}$$

where $x = L/X$, and $X = A/(\sigma_T \rho \mathcal{N})$ is the mean free path for scattering. On the other hand, the probability of a n-scattered K_L to stay in the beam is

$$P_B(n) = \frac{b}{n} dt = \frac{b p^2}{n \pi} d\Omega \tag{2.4.}$$

Hence, the number of detected K_L's in the transmitted beam is

$$N_T^{obs} = N_I e^{-x} \left[1 + d\Omega \, p^2 \frac{b}{\pi} \sum_{i=1} \frac{(ax)^i}{i \, i!} \right] \tag{2.5}$$

where $N_I e^{-x} = N_T$ is the true transmitted number of K_L's we want to measure.

(2) Scattering from one beam into the other

This is the following effect: K_L's may diffract from some beam line element (i.e. a collimator), or the absorber itself, into the other beam. If c is the probability for a K_L to scatter into the other beam, the number of observed decays are proportional to

$$N_T^{obs} = N_T + c N_I = N_T(1 + c e^x)$$

$$N_I^{obs} = N_I + c N_T = N_I(1 + c e^{-x}) \tag{2.6}$$

As c will be small, and x approximately 2, the correction to N_I will be neglected.

To calculate c, we simulated this beam "cross-talk" effect in a
Monte Carlo program. We found that in fact the main contribution came
from a 7.5 cm thick lead radiator located 35 m upstream of the
absorber. A verification of this was provided by plugging one beam
and observing diffracted events in it (See paragraph 6.3).

Combining the corrections (2.5) and (2.6), the true number of transmitted
K_L's is

$$N_T = N_T^{obs} \left\{ 1 + c\, e^x + d \Omega\, p^2 \frac{b}{\pi} \sum_{i=1}^{3} \frac{(a\chi)^i}{i\; i!} \right\}^{-1} \qquad (2.7)$$

where a, b, c are slowly varying functions of the momentum to be
determined self-consistently via the Glauber model (a,b), and a Monte
Carlo (c).

2.2. Regeneration measurement

The K_S regeneration process, i.e. the reaction $K_L + A \rightarrow K_S + A$ has the
feature that in exactly the forward direction the amplitudes from all
the nuclei in a macroscopic target add coherently, whereas the rate of
regenerated events is proportional to $|f-\bar{f}|^2 N^2 L^2$, as opposed to dif-
fraction regeneration, where the rate is proportional to $|f-\bar{f}|^2 LN$.
The forward coherent peak eliminates the necessity (and uncertainty)
of an extrapolation to t = 0. Although the indicent neutral K_L is not
measured, this coherent signal can easily be isolated if the regenerator
is located far enough away from the production target to define the
incident K_L direction accurately.

With a double beam, coherent K_S regeneration is measured by placing
a regenerator block in one beam, and an identical absorber block, far
upstream, in the monitoring beam to correct for absorbtion in the
regenerator (Fig. 2.2). In the decay region (i.e. in the vacuum pipe

located between the regenerator and the spectrometer), one detects
Kπ2 decays of K_S's behind the regenerator, and Kμ3 decays of K_L's from
the monitoring beam. Note that the blocks, and hence the functions
of the two beams are constantly interchanged.

The main advantage of the double beam method is that the Kμ3 rates
do not have to be corrected for diffraction in the regenerator, as
would be the case when detected directly downstream of it. For the
same reason, the Kμ3 sample does not have to be corrected for Kπ2's
with a pion decaying in flight.

The phenomenology of K_S-regeneration is well known[1]. One finds that
the intensity of $\pi^+\pi^-$ decays, behind a regenerator of thickness L is

$$I(K\pi2, \tau, p) = N_I \exp(-L/X) \, BR(K\pi2) \, \Gamma_S \Big\{$$

$$\left| \rho(p,L) \exp\left(-im_S\tau + \frac{1}{2}\Gamma_S\tau\right) + \eta_{+-} \exp\left(-im_L\tau + \frac{1}{2}\Gamma_L\tau\right) \right|^2 \Big\}$$

$$= N_I \exp(-L/X) \, BR(K\pi2) \, \Gamma_S \Big\{ |\rho|^2 \exp(-\Gamma_S\tau) +$$

$$2|\rho\eta| \exp\left[-(\Gamma_L+\Gamma_S)\frac{\tau}{2}\right] \cos\left[-(m_L-m_S)\tau + \phi_\rho - \phi_\eta\right] + |\eta|^2 \exp(-\Gamma_L\tau) \Big\} \quad (2.8)$$

where τ is the proper time elapsed between the exit from the downstream face
of the regenerator and the decay, and BR(Kπ2) the branching ratio of
$K_S \rightarrow \pi^+\pi^-$.

The regeneration amplitude $\rho(p,L)$ is connected with the forward amplitude
difference $(f-\bar{f})$ by

$$\rho(p,L) = i\pi N \left(\frac{f(0) - \bar{f}(0)}{p} \right) \frac{1 - \exp(iBL)}{-iB} \quad (2.9)$$

where

$$B = \frac{m}{p} \left[(m_L - m_S) - \frac{i}{2} (\Gamma_L - \Gamma_S) \right]$$ (2.10)

and

$$m = \frac{1}{2} (m_L + m_S)$$ (2.11)

and N is the number of scattering centers, $N = \mathcal{N}\rho/A$.

The contribution of the CP-violating $K_L \longrightarrow 2\pi$ decays is given by the momentum independent amplitude η_{+-}. Independent knowledge of this amplitude would allow, by a fit to the proper time distribution (2.8), to measure ρ. Because of the availability of the second beam for monitoring, we did not use this so-called "interference method", but rather the statistically much more powerful technique of observing the decay of the regenerated K_S's in the region where the $|\rho|^2$ term in (2.8) is dominant. This choice determined the length of the decay region, which was taken to correspond to two K_S-lifetimes at 100 GeV, i.e. 11 m.

For thin regenerators (i.e. BL $\ll$ 1), the expression (2.9) becomes

$$\rho(p, L) \cong i \pi N \left(\frac{f - \bar{f}}{p} \right) L$$ (2.12)

so that the leading term in (2.8) is proportional to

$$|\rho|^2 L^2 \exp(-L/x) .$$ (2.13)

This last expression maximizes at L=2X; therefore all our regenerators (and absorbers!) were chosen to be two kaon interaction lengths long.

For the monitoring beam, the rate of Kµ3 decays in the decay region is given by

$$I(K\mu 3, \tau, p) = N_I \exp(-L/X) BR(K\mu 3) \Gamma_L \exp(-\Gamma_L \tau) \qquad (2.14)$$

so that by taking absorbers and regenerators of same L one measures directly the incident number of K_L's, N_I.

At a given kaon momentum p, the limits of the decay region will correspond to the proper times $\tau_1(p)$ and $\tau_2(p)$. Thus the number of detected Kπ2 and Kµ3 decays will be

$$N(K\pi 2, p) = A(K\pi 2, p) \int_{\tau_1}^{\tau_2} I(K\pi 2, \tau, p) \, d\tau \qquad (2.15)$$

$$N(K\mu 3, p) = A(K\mu 3, p) \int_{\tau_1}^{\tau_2} I(K\mu 3, \tau, p) \, d\tau \qquad (2.16)$$

In this expression A(Kπ2, p) and A(Kµ3, p) are the detection efficiencies by the apparatus (<u>acceptance</u>) of the $K_S \rightarrow \pi^+\pi^-$ and $K_L \rightarrow \pi\nu\mu$ decays, <u>integrated</u> over the entire decay region. These acceptances, as defined in (2.15) and (2.16), will be calculated by a Monte Carlo program (See Chap. 5).

Let us now suppose that we know $\phi = \arg(f-\bar{f})$ and take for η_{+-} the measured value. The only unknowns left in (2.15) are thus $|f-\bar{f}|$ and the normalization factor $N_I \exp(-L/X)$. Dividing (2.15) and (2.16) we eliminate this later term and obtain an <u>equation</u> for $|f-\bar{f}|$.

As ϕ enters only in the (small) interference term, together with η_{+-}, it is sufficient to take it from a Glauber-Regge model in a self-consistent manner. In fact this model shows that even for heavy nuclei the dominant contribution to $f-\bar{f}$ is, as expected, the ω trajectory. ϕ is thus simply given by the phase of the ω Regge amplitude, i.e.[5].

$$\phi = \arg\left(f - \bar{f}\right) \simeq -\frac{1}{2}\pi\left[\alpha_\omega(0) + 1\right]$$

(2.17)

For the same reason, the uncertainty in η_{+-} will have only a small effect. Therefore, we obtain a virtually systematics-free measurement of the modulus $|f-\bar{f}|$.

We shall now examine various backgrounds and systematics affecting the regeneration signal ($K\pi2$ decays) and the flux monitoring ($K\mu3$ decays).

Backgrounds in the $K\pi2$ signal consist of leptonic decays which fake, over a limited kinematical range, $K\pi2$'s. $K\mu3$'s are effectively removed already at the trigger level by identifying the muons. $Ke3$'s can be reduced with the (off-line) requirement that the electromagnetic energy that is measured for each particle in a shower counter be inconsistent with its momentum as measured by the spectrometer. The $K\pi2$'s must also be corrected for diffraction regeneration. These diffracted K_S's have a much broader t dependence than the K_S's from the coherent peak. Together with the residual $Ke3$'s, the diffracted $K\pi2$'s result in a small, essentially flat background in the momentum transfer distribution, which can be substracted by extrapolation under the coherent peak to t=0 (See Fig.5.3).

Systematics in the $K\mu3$ decays used for flux monitoring are as follows:
(a) The branching ratio $K_L \longrightarrow \pi\mu\nu$ is known only to $\pm2\%$. This induces an averall normalization uncertainty, but will not affect conclusions as to momentum or atomic number dependence; (b) $\pi-\mu$ decays in flight of other decay modes may simulate $K\mu3$ decays. The contribution of these at the trigger level was about 5%, with $Ke3$ with π-decay in flight dominating.

This background will be corrected by Monte Carlo; (c) The Kμ3 have to be corrected for diffraction scattering in the absorber, and for scattering from one beam into the other. This correction was the same as for the total cross-section measurement, i.e. (2.7) .

2.3. η_{+-} measurements

As the apparatus detects simultaneously Kπ2 and Kμ3 decays from both beams, the Kπ2 yield in the monitoring beam allows a measurement of η_{+-}. From (2.8) with $\beta=0$, and (2.15, 2.16) one gets easily

$$\frac{N(K\pi2, p)}{N(K\mu3, p)} = \frac{BR(K\pi2)}{BR(K\mu3)} \frac{A(K\pi2, p)}{A(K\mu3, p)} \frac{\Gamma_S}{\Gamma_L} \left| \eta_{+-} \right|^2 \qquad (2.18)$$

As both decays come from K_L's in the absorbed beam, the correction (2.7) drops out in this case.

The determination of η_{+-} provides a consistency check of the experiment and can serve as an indicator of the systematic uncertainty due to the use of the Kμ3 normalization.

3. BEAM LINE AND SPECTROMETER

3.1 Beam line

This experiment was performed in the M4 neutral beam at Fermilab. Fig. 3.1 shows the main components of the beam line and Fig. 3.2 the spectrometer. The beam, consisting of neutrons, gammas and kaons, was produced by bombarding a 0.16 cm x 0.16 cm x 20 cm Be target with 400-GeV protons. The distance from the target to the regenerator (516 m or $\geqslant 80\, \Lambda_S$) insures the total absence of any K_S's.

The production angle (7.25 mrad) and the sizes of the two beams are determined by a fixed collimator 113 m from the production target. This 1.22 m thick steel collimator has two 1.27 cm x 1.27 cm holes, separated by 0.32 cm, defining two 5.8 cm x 5.8 cm beam spots, on top of each other, at the regenerator. Further control is provided by remotely adjustable collimators, at 202 m and 312 m. Each of these 1.22 m thick steel collimators are preceded by a 1.22 m long copper slab, respectively 0.57 cm and 0.89 cm wide, insuring a perfect separation of the two beams.

The final beam spot sizes during normal running were approximately 5.75 cm x 5.75 cm square with a vertical separation of 1.3 cm.

Sweeping magnets located immediately downstream of each adjustable collimator insure that only neutral particles enter our apparatus. Evacuated beam pipes, equipped with mylar vacuum windows, were placed through all long streches of the beam line, to minimize the interaction of particles with air.

A lead converter at 79 m served to suppress gammas in the beam. This converter, entirely mounted within a sweeping magnet, consisted of twelve 0.64 cm thick slabs of lead, each spaced approximately 5 cm apart. The magnet provided continuous sweeping of the shower produced along the length of the radiator. With the lead radiator in place, the beam at the apparatus consists of K_L's and neutrons, in the approximate ratio 1 : 5.

A neutron counter telescope, located approximately at 200 m, just before the first adjustable collimator, provided a relative beam monitor. This neutron monitor consisted of a veto counter, followed closely by a neutron converter (1 cm Al), and by two counters (separated by 1.2 m) in coincidence. The ratio of the neutron monitor ("NM") to a secondary emission monitor ("SEM") of the incident proton flux provided a reliable continuous measure of the targetting efficiency. Furthermore, a slow-sweep oscilloscope display of suitably integrated neutron monitor pulses revealed the time structure of the beam spill, including large spikes during which the electronics was gated off.

A measurement of the K_L spectrum from 30 to 130 GeV/c appears in Fig. 3.3. We observed 5×10^5 K_L's total per 10^{12} 400-GeV protons on the target, which was a typical intensity. This spectrum was obtained from the observed Kμ3 decays in vacuum, and corrected for the detection efficiency of our apparatus.

3.2. Targets

The C, Al, Cu, Sn and Pb targets were chemically pure, naturally occuring isotopic mixtures. They were carefully machined blocks, with thicknesses chosen to be of about two kaon interaction lengths, and such that each pair of absorber and regenerator had precisely the same length. The densities of the targets were checked by two independent methods in order to make sure that no holes were hidden inside. The physical parameters of our targets are listed in Table 3.1.

3.3. Absorbers (upstream target)

The absorbers were located immediately downstream of the fixed collimator at 114 m from the production target. All the different absorbers were mounted on a "revolver"-style moving machine which, under remote control, was able to rock a selected target from one beam into the other one (see Fig. 3.4.). A special "half-length" Sn absorber was included in order to study possible systematics in our total cross-section measurement method.

As the beam spot size was only of 1.3 cm x 1.3 cm at this position the absorbers could be made relatively light-weight so that the mecanical design of this machine was easy. However, because of the limited access to this high radiation enclosure of the Meson Laboratory, the machine had to be made very reliable, and its electronics radiation hardened.

3.4. Regenerator (Downstream target) and sweeping magnet

The regenerator was placed within a magnet, to sweep out locally produced charged particles. To contain the beam spot amply the regenerators were of 7 cm x 7 cm cross-sectional area. The mecanical constraints on the machine needed to displace such a block weighing 10 to 15 kg within the 10 cm x 18 cm magnet gap were quite severe. The design allowed a given target to be translated from one beam into the other one in 3 to 4 seconds, which was fast enough to alternate the function of the beams on a burst-by-burst basis (see Fig. 3.5.). The longitudinal position of the regenerator inside the sweeping magnet was optimized in order to be as close as possible to the entrance window of the decay pipe so as to detect as many regenerated K_S's as possible.

3.5. Anti-counter and decay region

An anti-counter (C1) was installed between the sweeping magnet and the entrance window of the decay pipe to veto the charged particles, insuf-ficiently swept by the magnet. This anti-counter consisted of a 1.6 mm thick, 18 cm x 8 cm in size, scintillator viewed by a RCA "Quantacon" phototube. In order to handle the very high counting rate, the photomultiplier gain was set to deliver only small pulses; these had to be further amplified before driving a fast updating discriminator.

The entrance vacuum window of the 1I m long decay pipe was a .13 mm thick mylar window, and the residual pressure ($<35 \mu$m Hg) in the pipe was

carefully monitored so that multiple scattering and secondary interactions
(i.e. regeneration) were negligible.

3.6. Trigger counters

The arrangement of the scintillation counters was chosen with the following
criteria :

1.) A neutral particle should enter the decay pipe and decay into a charged
"V" within it.

2.) A candidate "V" has two and only two tracks, and they are roughly right-
left symetric.

3.) Accidental rates should be minimized.

4.) The amount of matter within the spectrometer should be minimal.

We shall elaborate on these aspects of the trigger below.

To insure condition (1), an anti-counter (C1, already described) was placed
immediately downstream of the regenerator, and a MWPC (MF) was placed
immediately downstream of the decay pipe exit window. C1 was large enough
to cover the area of the regenerator in its two positions and had high
efficiency to veto charged particles produced in the regenerator. The
proportional chamber MF, 86 cm x 43 cm in area, constituted a massless
counter. Its fast output was required in coincidence.

The basic two tracks trigger was defined by two vertical counter hodoscopes:
C2, near the front MWPC table, and C3, downstream of the back table. Each
hodoscope was logically divided into left and right halves, centered on
the beam line. A track on the left (right) side of the apparatus was thus
given a signature in each bank C2L (C2R), C3L (C3R). Each half of C2
consisted of 12, 7.5 cm x 35 cm scintillators 1.6 mm thick, arranged 6
above and 6 below the beam line, C2 thus defined four quadrants. The

thickness of the C2 elements, and their wrapping, were chosen so as to minimize multiple scattering. C2 was used in a majority logic so that one and only one element on each side (R, L) was required to fire.

C3, which consisted of 24 vertical strips 5 cm x 122 cm x 0.67 cm in size, was located downstream of the last proportional chamber and therefore could not deteriorate the resolution.

C4 was essentially identical to C3, except that its strips were horizontal, and its main purpose was to reduce the accidentals. Only one hit in C4 was required, since some of the events had both their tracks in a nearly horizontal plane.

The basic two-track trigger defined by the above counters was thus:

$$P2 = \overline{C1} \cdot MF \cdot C2L \cdot C2R \cdot C3L \cdot C3R \cdot C4$$

All the neighboring counters within the hodoscopes were arranged to overlap by about 1.5 mm in order to avoid "cracks" that would have spoiled the uniformity of the geometrical acceptance. The only exception was the left-right separation in C2 and C3 which resulted in a 4-mm wide vertical gap centered on the beam axis.

3.7. Particle identifying counters

In addition to the trigger counters above, special counters were employed to identify the electrons from Ke3 decays and the muons from Kμ3 decays.

An array of 12 overlapping lead-lucite shower counter units (SC), 60 cm x 20 cm each, were placed downstream of C4. Each unit consisted of 15 sheets of lead (15 radiation length total) interspersed with 16 sheets of lucite (1 radiation length total) mated smoothly to an adiabatic lucite light collector. All SC's were identical, except for two of the central units through which the beams passed, which had a 3 cm x 3 cm hole to avoid interaction with neutrons in the beam.

The excellent electron identification provided by this SC has been extensively used in the analysis of the two previous regeneration experiments performed in the same beam line[5,14]. The much cleaner background situation of the present experiment (mostly because of the relatively shorter decay region), did not necessitate to use the SC's other than for background study purposes.

In front of the lead-lucite shower counter was a 2 radiation length "thin" shower counter. This second electron identifier was made out of two halves, left and right, each of them consisting of two 110 cm x 60 cm x 0.6 cm sheets of lead, immersed in a tank of liquid scintillator viewed by 4 photomultipliers. The output signals of each of these counters was recorded by ADC's, just like the other "thick" shower counters, but the former signals were also summed, on the left and on the right, to provide, after discrimination, a real-time electron veto signal. This feature was used to suppress Ke3 decays in a special run intended to measure the CP violating K_L to 2 pions decay branching ratio.

The muon counter, C5, consisted of approximately 3 m of steel (16 pion absorption lengths and a muon range of 2.5 GeV), followed by a hodoscope (C5) consisting of twelve vertical 16 cm x 160 cm x 1.3 cm scintillators overlapped by about 2 cm. The pion "punch through" probability was negligible. The C5 outputs were stored for each event so that the spatial information could be used off-line to identify which of the two tracks belonged to the muon. Because of the multiple scattering of the muons in the steel this identification was not always unambiguous. We therefore calculated the probability for either track to have hit the struck counter(s) and identified the muon as the track having the highest probability. C5 entered the trigger in coincidence for Kμ3 triggers, and in veto for Kπ2 triggers. Since the normalization was done in this experiment relative to Kμ3 decays, the efficiency of C5 had to be regularly checked in special runs; in these the beam block was closed so that only genuine muons could reach the spectrometer. Using a single track trigger it was then easy to measure the absolute efficiency of the C5 counters and to study the muon identification procedure.

3.8. The analysing magnet

The analysing magnet used in the experiment had an average field set to provide a transverse momentum kick of 206 GeV/c. This value, which equals the momentum of the pion in the two pion decay mode, maximizes the acceptance ratio of the Kπ2 to semi-leptonic decays.

The field integral was measured with a flip-coil magnetometer at every point on a 7.5 cm grid in the transverse plane throughout the region defined by the trigger counters, and longitudinally from -90 cm to +90 cm. The field was highly uniform (varying by less than 2.5%) through the area defined by the trigger counters, while its stability with time was better than 0.1%. A non-negligible horizontal field component, corresponding to a few MeV kick in the non-bending projection, was measured and corrected for in the analysis. The magnet gap, 66 cm, defined the vertical acceptance of the spectrometer.

3.9. Multiple-Wire Proportional Chambers

The five MWPC's used in the experiment were of the now common variety Charpak chambers and had a 1.6 mm (1/16") wire spacing and a 4.8 mm (3/16") cathode to anode gap. The sensitive areas of the chambers were : 60 cm x 120 cm for the 3 front chambers, and 95 cm x 140 cm for the 2 back chambers.

The chambers were continuously flushed with a mixture of 80 % Argon, 20 % CO_2 and 0.25 % of Freon.

The efficiency of the chambers was plateauing at 3.8 to 4.0 kV, and the plateau was about 200 to 300 V long. In between the beam spills, the high voltage was lowered by a few hundred Volts in order to keep the dark current low and save the chambers. During the spill, the dark current was typically of 1 to 3 μA. The normal chamber strobe width was 50 ns wide, and the timing curves were typically 90 to 120 ns wide.

Four of the chambers consisted of x, y planes each, while the second chamber in the spectrometer had its wires slanted at 45° (u, v, planes).

The vertical plane of the third chamber in the spectrometer was split into separately read-out left and right halves. This served to remove left-right ambiguities. The dead region at the split was only about 5 mm wide.

The 8000 wires of the spectrometer were read-out by a fast priority encoding read-out system that will be described in paragraph 4.3.

3.10 Component list

In table 3.2 we list all the elements in the spectrometer, relevant dimensions and thicknesses in radiation lengths. The radiation length of most elements in this table contains a contribution from the surrounding air. To minimize it, all the free regions between the detectors, and the magnet gap, contained helium bags.

4. TRIGGER LOGIC AND DATA ACQUISITION

4.1. Trigger electronics

The fast logic used in the experiment consisted almost entirely of standard NIM modules. A schematic of the trigger circuitry and of its interconnection with the camac is shown in Fig. 4.1. The fast decision was taken on two successive levels.

The first level consisted of the coincidence

$$C2 = \overline{C1} \cdot C2L \cdot C2R$$

which was latching the information of all the hodoscopes into the camac pattern units. Then the two-track trigger was built up as

$$P2 = (C2 \cdot MF) \cdot (C3L \cdot C3R \cdot C4)$$

The basic signature of the $K\pi2$ and $K\mu3$ decays were thus given by

$$KPI2 = P2 \cdot \overline{C5}$$

and

$$KMU3 = P2 \cdot C5$$

The much more abundant KMU3 triggers were usually prescaled down by 2, 4 or 8 and ored with the KPI2 signals to define an event candidate (EVENT).

The second level made use of specially designed combinatorial ECL circuit which provided an exclusive signal insuring that, save for left-right and up-down overlaps, there was one and only one hit on either side of the C2. This exclusive signal C2 was generated from the C2 hodoscope

information latched at the first trigger level. Its purpose was to veto the strobing of the proportional chambers in case of a (background) trigger producing a multi-hit configuration in C2. Thus the coincidence EVENT $\cdot\overline{C2X}$ produced a valid event interrupt and initiated the strobing of the MWPC's and ADC's, while the condition EVENT$\cdot$C2X + $\overline{EVENT}\cdot$C2 resulted in an early reset of the pattern units.

The first-level trigger rate was typically of about 10^4 per beam spill, while the usual data taking rate was around 200 - 300 events per beam spill, being essentially limited by the data-acquisition system buffer size.

4.2. Camac electronics

All the real time information was interfaced to the on-line computer via a camac system. The event, beam spill and other synchronisation interrupts were fed into a CERN-designed "Look-at-me" grader[8] which also generated the dead-time signals inhibiting the trigger logic. The camac contained pattern units for the 112 bits of hodoscope information, event flags and moving-machine status bits. For the shower counter information 20 ADC channels of 8 bit resolution were recorded per event. At the end of every beam spill 32 camac scalers were read out to monitor various rates and to record the SEM and the neutron monitor (NM). The neutron-monitor signal was also recorded in anti-coincidence with the total dead time (NM*), so that the ratio NM*/NM gave a direct measure of the true live time (see Fig. 4.1.).

4.3. MWPC readout

The MWPC read-out was making use of a fast priority encoding scheme designed by T.A. Nunamaker[9]. All the chambers were read out simultaneously under control of so called "coupler boxes", one for each chamber plane, which contained a buffer for up to 16 fully encoded wire addresses.

The wire information was first strobed by the event trigger into a shift register which latched the struck wires. The latched wire information was ored into subgroups of 8 wires and then into groups of 64 wires. The priority encoders, distributed along the chamber plane, found in sequence the group, then the subgroup containing the highest priority struck wire (i.e closest to the coupler box). The 8 bits of shift register containing this wire was then transmitted to the coupler box which calculated its address.

The full process of encoding a struck wire took less than 2 microseconds; so that, in principle, the full MWPC system was available in less than 10 microseconds for recording a new event. But, in our experiment, this double buffering capability was not used.

The buffered wire addresses were finally sent serially to a camac scanner which was reading out, under program control, the 10 chamber planes sequentially at a rate of about 20 microseconds per wire address.

4.4. Data acquisition computer

The on-line computer was a 32 K, 16 bit, Data General "Supernova". The memory cycletime was 800 ns and the computer was equipped with a fast floating-point unit, a 256 K fixed head disk and a 800 bpi 75 ips tape drive.

The raw data, acquired via camac during the 1 second beam spill, were buffered in a 16 K, 16 bit fast external stack so that the full memory was available for programs.

The function of the computer during the beam spill was restricted to the read-out of the camac under program control. The read-out dead time was of the order of 400 to 800 microseconds per event because the computer was used to compact and check the data while reading it in. For instance, a minimum and maximum number of struck wires was preset and the computer rejected directly the events falling out of this range.

4.5. On-line pattern recognition

The prime design specification of the on-line computer system was to be able to reconstruct all the events completely ($\sim$ 250/burst!) in real time. The motivation was that one could use the 10 seconds between beam bursts to process the data. Indeed, it was found that the off-line processing of the data on a CDC 6600, using the same highly optimized algorithm, was only two times faster than on the Supernova. The reason is that simple pattern recognition programs make only minimal usage of the resources of large general purpose computers, so that the execution time depends ultimately only on the main memory cycle time.

The on-line program had several subroutines, first debugged in Fortran, and then translated into assembly code in order to make best usage of the Supernova features. The main steps of the on-line pattern recognition program were the following :

(1) An event was retrieved from the hardware stack and unpacked. Extensive diagnostic display of the detectors' performances was made at this level (see paragraph 6.1).

(2) The pattern recognition started by looking for straight tracks in the side-view projection in which the trajectories of the particles are essentially not bent by the magnet. The tracking road width was of 4 wire spacings, and the program allowed for 1 intermediate plane to be missing.

(3) Having found at least two tracks in the side view, the program proceeded by using the slant chamber to find 1 or 2 points of the tracks in the top-view. The split chamber was used already at this level to make sure that the event was not ambiguous by looking that it did not have both tracks on the same (left or right) side.

(4) The tracking in the top view started at the front of the magnet where usually the side-view information, linked by the slant and the split chambers, allowed the first front track segment to be found right away. The search road width was 4 wires wide.

(5) The track segment candidates found at the front were next extended to the magnet center plane were their intercepts provided a pseudo-plane for tracking at the back of the top-view.

(6) The back track segments were found by tracking for straight lines using as one end-point the pseudo-plane in the center of the magnet. The road width was 2.5 wires.

(7) The final step in the top-view tracking was to find two pairs of segments, matching within 2.5 wires at the center of the magnet, defining two bent tracks with a vertex upstream of the first chamber.

The reconstitution efficiency was between 55 % and 65 % of the triggers, depending on the running conditions. It was as high as 75 % for KMU3 triggers which generally had a cleaner signature than the KPI2's. This reconstruction efficiency was our best monitor of the apparatus. It was displayed at the end of every beam spill and dropped immediately in case of a hardware problem.

The unsuccessful events were either non-reconstructable because of an obvious defect, or ambiguous. This second class, of about 5 %, consisted mostly of multi-prong events, or events for which it was not possible to find a unique solution to the tracking. The ambiguous events were discarded in the final analysis.

The throughput of the on-line system was of 150 to 250 events per pulse, and usually a few events were left in the buffer at the beginning of the following beam spill, at which time they were discarded to read in new data.

An off-line production program fitted a second order spline to the found tracks in both views, calculated their momenta using the field map, and wrote a compressed data tape summarizing the kinematical parameters of the events.

Although the "raw" MWPC hits were also recorded, in parallel, onto the on-line tapes, the output of the "real-time" pattern recognition was final, and never had to be reconsidered.

5. MONTE CARLO AND CUT PROGRAMS

5.1. Monte Carlo program

In order to obtain the number of Kπ2 and Kμ3 decays that actually oc-
cured in the decay region, the probability for a Kπ2 or Kμ3 to be ac-
cepted by the spectrometer is needed. This probability, which is called
the acceptance of the apparatus, is calculated by a Monte Carlo (M.C.).

In principle the acceptance of the apparatus for a given decay mode is a
function of the kaon momentum and of the vertex of its decay point. However,
for the purpose of this experiment we can assume the Kπ2 and Kμ3 proper
time distributions to be known. It is therefore sufficient to calculate the
Kπ2 and Kμ3 acceptances integrated over the entire decay region according
to the definitions (2.15) and (2.16).

In calculating the acceptance, Kπ2 and Kμ3 events were generated with
the complete physics, and the action of the apparatus was simulated in all
respects. That the Monte Carlo program was indeed successful was tested by
comparing real data and M.C. for distributions which are sensitive to pro-
blems that would influence the calculated acceptance.

In order to simulate resolution effects which would cause events to migrate
from one bin to another (either in momentum, or any other variable) as
closely as possible, the M.C. kaons were generated with approximately the
observed momentum spectrum (Fig. 3.3). The real transverse beam dimensions
were used an K_L's were generated at random in one beam or in the other.
Next, they were made to decay in a volume starting exactly at the anticounter
C1 and ending at MF. Kπ2 decays were generated according to the decay low
(2.8), while Kμ3 events were generated according to a flat distribution in
proper time.

In the Kπ2 decay of the kaon, the pions were distributed on a unit sphere with a momentum 206 MeV/c. For Kμ3 decays, the energies E_μ and E_π were generated on a Dalitz plot with a density given by the matrix element[10]:

$$\frac{d^2N}{dE_\pi \, dE_\mu} \propto f_+^2(t) [A + B\xi + C\xi^2]$$ (5.1)

$$A = m_K (2 E_\mu E_\nu - m_K E'_\pi) + m_\mu^2 (\frac{1}{4} E'_\pi - E_\nu)$$

$$B = m_\mu^2 (E_\nu - \frac{1}{2} E'_\pi)$$

$$C = \frac{1}{4} m_\mu^2 E'_\pi$$

$$E'_\pi = \frac{1}{2} (m_K^2 + m_\pi^2 - m_\mu^2)/m_K - E_\pi$$

$$t = m_K^2 + m_\pi^2 - 2 m_K E_\pi \quad , \qquad m_K = E_\pi + E_\mu + E_\nu$$

where $f_+(t)$ was parametrized as

$$f_+(t) = 1 + \lambda t/m_\pi^2$$ (5.2)

with λ=0.0314 and ξ=-0.11 .

The momenta of the charged particles were than Lorentz-transformed to the laboratory frame, and the tracks traced through all the elements of the spectrometer.

Multiple scattering was simulating in each element listed in table 3.2. As the matter in the spectrometer was on the average mostly of low Z material (Mylar, plastic scintillator, air, ...), we used the Molière theory[11] to generate a standard angular distribution corresponding to .005 radiation lengths of carbon. This standard distribution was sampled at random, and the actual deflection was obtained by scaling the sample θ_0 by the factor[12]

$$\theta/\theta_0 = \frac{0.015}{p} \sqrt{x} \left[1 + \frac{1}{9} \log_{10}(x)\right]$$ (5.3)

where x was the thickness in radiation lengths of the given spectrometer element. The Molière correction was found to be significant for the thin elements of our spectrometer.

The pions were allowed to decay anywhere in the spectrometer. The resulting muons, distributed isotropically in the center-of-mass of the pions, were Lorentz-transformed to the laboratory frame.

The bending of each track through the analysing magnet was calculated using the actual field map. A small bending in the vertical plane, due to a non-negligible horizontal field component, was also allowed for.

The muons were allowed to pass through the muon-filter with the proper amount of multiple scattering generated with the complete Molière formula. Hits in C5 were recorded and actual counter inefficiencies (as measured with special muon runs) were allowed for.

Counter boundaries, with the same dimensions and locations as the experiment were used and struck counters were recorded for later use.

The intercepts of the tracks in the read-out planes were "digitized" to reproduce the discrete spatial information given by the wire chambers. When a track intercept was approximately equidistant from two wires, this digitization included the simulation of adjacencies (spreads). Thus, one or two wires near each track position were struck according to the observed frequency, and then "struck wires" (allowing for measured chamber inefficiencies) were stored for later analysis, just as the actual proportional chambers hits.

Only very basic geometric cuts (simulating the action of the trigger electronics) were included in the M.C. These were C2 boundaries, C3 boundaries, and a requirement in C2 and C3 that one track lie on the left side, and one on the right. Furthermore, to simulate the cuts introduced by the on-line reconstruction program, the stored chamber hits were checked to lie within the "roads" used by the pattern recognition program, and

events that would not have been reconstructed were rejected. If the events survived these basic cuts, they were written onto tape in the same format as the on-line data tapes, to be processed by the same cut program.

We shall now discuss various studies performed to ascertain that the resolution of the apparatus was well understood.

Of particular interest was whether the M.C. program correctly simulated the data in its treatment of chamber digitization and multiple scattering. "Deviation histograms" were obtained by connecting a straight line between the first and the last hit of a track in the side view, and then plotting the deviation of each hit from this line in the intermediate planes. These histograms served mainly as a monitor of consistent operation, since multiple scattering contribution to the resolution is comparable (as was found) to the digitization contribution.

Since the deviation due to the multiple scattering has $1/p$ dependence, while the contribution from digitization is momentum independent, we can, by binning the squares of the deviations versus $1/p^2$, separate the two effects. Fig. 5.1. shows such a plot, and from the slopes of the lines we see that the agreement with M.C. in the multiple scattering is of the order of 10 %.

The degree of agreement between the M.C. simulation and real data is ultimately reflected in the comparison between observed distribution of kinematical quantities, and those predicted by the M.C.

Let us define the "visible momentum" and the "visible energy" of the decays by

$$\vec{P}_v = \vec{P}_1 + \vec{P}_2 \quad , \quad E_v = E_1 + E_2 \tag{5.4}$$

where the labels 1, 2, refer to the two charged tracks, interpreted as pions or muons. The "good geometry" of the spectrometer allows us to define the incident direction of the beam by a unit vector $\vec{u}$. Thus, the

visible momentum can be decomposed into longitudinal and transverse components

$$\vec{P_v} = \vec{P_\ell} + \vec{P_t}$$ (5.5)

such that

$$P_\ell = |\vec{u} \cdot \vec{P_v}| \quad , \quad P_t = |\vec{u} \wedge \vec{P_v}|$$ (5.6)

For Kπ2 decays, one kinematical quantity of interest is precisely the squared transverse momentum of the kaon, p_t^2. Another is the invariant mass

$$m_{\pi\pi} = E_v^2 - P_v^2$$ (5.7)

where both prongs of the "V" are interpreted as pions. A typical $m_{\pi\pi}$ distribution is shown in Fig. 5.2., and a p_t^2 distribution in Fig. 5.3. By binning the data and the Monte Carlo in 10 GeV wide momentums bins, one can study the momentum dependence of the $m_{\pi\pi}$ distribution variance, and of the p_t^2 distribution logarithmic slope. Fig. 5.4 and Fig. 5.5 show a data-M.C. comparaison of these two quantities.

Since the neutrino in Kμ3 decays are not observed, the kaon momentum $\vec{P_K}$ is not exactly calculable for these events. But, as we know the incident direction, there are only two solutions for the three-body decay :

$$\vec{P_K} = \vec{P_0} \left(1 \pm \sqrt{ARG} \right)$$ (5.8)

were the average of the two solutions is

$$\vec{P_0} = \vec{P_\ell} \left(m_K^2 - P_v^2 + E_v^2 \right) / 2 \left(E_v^2 + P_\ell^2 \right)$$ (5.9)

and the argument of the square root is

$$ARG = 1 - \left[1 - E_v^2 / P_\ell^2 \right]\left[1 - \left(\frac{2 E_v m_K}{m_K^2 - P_v^2 + E_v^2} \right)^2 \right]$$ (5.10)

These two solutions correspond to the longitudinal components of the neutrino momentum being forward or backware with respect to $\vec{p}_K$. In the limit of purely transverse neutrino momentum, those two solutions become equal and we may call the event an "unambiguous" Kμ3 . A typical distribution of ARG is shown in Fig. 5.6. In this distribution, unphysical events with ARG<0 occur because of the finite resolution.

5.2. Cut program

For the final selection of events to be used in the analysis, a cut program was used that applied (as far as appropriate) the same cuts to real and M.C. Kπ2 and Kμ3 data.

The general type of cuts were the following :

(1) Geometrical cuts :

- A 2.6 cm wide vertical strip was cut out at C2 in order to avoid possible misreconstruction because of the splits in C2 and chamber 3.

- A ±61 cm, horizontal and vertical aperture cut was applied at C3 to reject events reconstructed with a track outside of its aperture.

- Events with two tracks on the same side of C3 were rejected.

(2) Vertex cuts :

- To suppress background events generated by interactions in the downstream window of the decay pipe, the vertex of the event was required to be at least 40 cm upstream of it.

- The half distance of closest approach of the two tracks divided by the distance of the vertex to the first MWPC had to be $\lesssim$ .0003. This cut insured the quality of the vertex.

(3) Momentum cuts:

- All events with any track momentum below 10 GeV/c were eliminated. As the range of muons in the muon filter was of 2.5 GeV, this cut insured that no muon had to low an energy to penetrate the steel. Also, as the resolution of the spectrometer was quite sensitive to the multiple scattering, this 10-GeV cut minimized possible problems in the simulation of this effect.

- Events with both particles of the same sign of charge were rejected.

(4) Kinematical cuts :
- The invariant quantity[13]

$$\left(p_0' \right)^2 = \left[\left(m_0^2 - m_K^2 - m_\pi^2 \right)^2 - 4\, m_K^2\, m_\pi^2 - 4\, m_0^2\, p_t^2 \right] / 4 \left(p_t^2 + m_\pi^2 \right) \qquad (5.11)$$

were m_0 is the mass of the π^0 and m_π the mass of the charged pion, is strictly positive for $K\pi3$ decays. By requiring

$$\left(p_0' \right)^2 \leq -5 \left(MeV/c \right)^2$$

one rejects completely all the $K\pi3$'s.

- For $K\pi2$'s the invariant mass $m_{\pi\pi}$ was required to be within 20 MeV of the kaon mass :

$$\left| m_{\pi\pi} - m_K \right| \leq 20\ MeV$$

- For $K\mu3$'s, the "unambiguous" cut on the argument distribution was set at

$$\left| ARG \right| \leq 0.01$$

From (5.8) this cut implied that for the accepted $K\mu3$ decays, the two solutions did not differ by more than $\sqrt{ARG} = 10\ \%$ from their average.

5.3. Background substraction

Looking at the Kπ2 momentum transfer distribution in Fig. 5.2, one sees that the coherent signal is confined to the region $p_t^2 < 500$ (MeV/c)^2. Thus, the region $p_t^2 > 500$ (MeV/c)^2, can be used to estimate the amount of background (diffracted K_S's, Ke3's, inelastic events,...) under the coherent peak. Assuming that this background is _flat_, we used the following very simple background substraction recipe :

$$N(K\pi2,p)\Big|_{corrected} = \int_0^{500} dp_t^2 \frac{dN(K\pi2,p)}{dp_t^2} - \int_{500}^{1000} dp_t^2 \frac{dN(K\pi2,p)}{dp_t^2} \qquad (5.12)$$

As this technique was also removing some good events (scattered by the resolution) from the coherent signal, we applied the same formula to the M.C., so that the calculated Kπ2 acceptance included the losses due to this background substraction. In the analysis section we shall present several checks of the correctness of this procedure.

For the Kμ3 decays in the monitoring beam, having removed all the Kπ3's, the only substantial source of background left were the Ke3 decays with the pion decaying in flight. This background was calculated with the Monte Carlo by replacing the muon in the three body decay section by the electron. Letting A(Ke3,p) be the probability for a Ke3 (with the pion decaying in flight) to be accepted as a Kμ3 decay, the corrected number of Kμ3's in thus

$$N(K\mu3,p)\Big|_{corrected} = N(K\mu3,p)\left[1 - \frac{BR(Ke3)}{BR(K\mu3)} \frac{A(Ke3,p)}{A(K\mu3,p)}\right] \qquad (5.13)$$

5.4. Acceptances

The acceptances (integrated over the decay region) calculated by the Monte Carlo program, including all the cuts, are given in table 5.1. A(Kπ2,p) and A(Kμ3,p) are graphically displayed in Fig. 5.7 and Fig. 5.8.

6. DATA COLLECTION AND ANALYSIS

6.1. Spectrometer tuning and calibration runs

As the pattern recognition was done in real time, the full apparatus had to be first understood and optimized. This preliminary phase consisted in taking samples of data that were written onto tape to be rescanned by the on-line reconstruction program.

The first samples were of single track muons, taken with the beam block closed and the analysing magnet off, which allowed the coordinates of the MWPC's to be aligned. The MWPC's were timed in and plateaued with these straight-through muons, and the on-line computer calculated their efficiencies and spreads (i.e. the average number of adjacent wires that fired par track). The chamber efficiencies were above 98 %, except for the slant chamber which was only about 95 % efficient, and the spreads were typically around 1.20. The counter efficiencies were also measured with straight through muons. C5 was 98.7 % efficient, C4 and C3 above 98 %, but C2 (a much thinner hodoscope) was only about 95 % efficient with some counters as low as 90 %. The C5 efficiency was particularly watched because it affects directly the Kμ3 normalization. For this purpose, special muon runs with the magnet on were taken at the beginning and at the end of the main data taking period. The C5 efficiency was found to be stable at 98.7 % and showed no appreciable momentum dependence above 10 GeV/c. The "roads" used in the pattern recognition program were determined by rescanning various samples of two-track data, until an optimum was found : the roads had to be wide enough to allow for multiple scattering, but also narrow enough to be able to resolve track projections which were close to one another. The pattern recognition algorithm was than certified by studying the reconstruction efficiency. Lost events were plotted on a storage oscilloscope screen, and explained to come from an obvious

defect (missing chamber hits, false triggers, multiprong events,...) or
to come from well-understood and unbiased limitations of the program
(tracks to narrow to be resolved, non unique solutions, too complicated
events, ...). Further studies were made on larger samples (i.e. about
10^5 events), to insure that these losses were neither momentum dependent,
nor a function of the decay vertex position. The on-line program was
than "frozen" for the full experiment, and although a few small software
"bugs" were later discovered, their effect were included in the Monte
Carlo rather than corrected during data taking.

During all data runs, a number of checks were made by means of the
on-line program to insure proper and consistent operation of the equip-
ment. Monitoring the efficiency of the MWPC's amd counters was parti-
cularly important. For the chambers, this was done by histogramming the
frequency of hits in each plane, which for "V's" was peaking at 2. After
their initial timing-in and plateauing, the counter hit frequency
allowed their efficiency to be monitored relatively to one another. A
full diagnostic of one of the MWPC planes was done in turn for every run.
This included a full illumination plot and various histograms in groups
and subgroups of wires to display possible defects of the readout elec-
tronics.

The reconstruction efficiency itself was of course a sensitive monitor
of hardware problems, which were detected, without any delay, by a
decrease in the event retrieval.

The total number of hits in the MWPC's was also a "global" monitor of
the apparatus. With 10 chamber planes, and 2 tracks in each, a
"perfect event" is one in which there is a total of 20 wire hits
(see Fig. 6.1.). Studying the distribution (sharply peaked at 20) of
the number of hits per event, it was found that events with less than
16 hits were never reconstructed, and those with more than 48 were

mostly background. Both kinds were rejected at the input level by the data taking program, in order to save space in the buffer, and time for reconstructing "cleaner" events.

Finally, various scaler rates were monitored continuously. These were sensitive indicators of the various problems that would not necessarily show up on the on-line computer diagnostic outputs. The scaler rates monitored quantities such as beam intensity, targetting efficiency, deadtime of the apparatus, various accidental rates, as well as the efficiencies of various trigger elements.

6.2. Total cross-section data

The data for the total cross-section measurement was taken in the configuration described in paragraph 2.1, with the muon counter C5 required in the trigger. Thus Kμ3 decays in the decay pipe were detected.

In table 6.1. we summarize for all the targets various number of events from the trigger level to the final data sample after all the cuts. The targets included C, Al, Cu, Sn and Pb, the length of which were of about two interaction lengths, and one so called "half-length" target of about one interaction length of Sn, for systematics studies.

In order to investigate the scattering from one beam into the other, data were taken without any absorber but with one of the holes in the fixed collimator carefully plugged, for several thicknesses of lead radiator (0, 2.5 cm, 5 cm, and 7.5 cm).

After reconstruction, it was crucial that we know from which of the two beams the K_L decayed. Figure 6.2 shows a vertical profile of the reconstructed vertex position showing that one can associate each event

with a particular beam with negligible ambiguity.

One interesting check was of course to verify that the "double beam" technique did indeed lead to the cancellation of rate effects. As the two beams were at slightly different production angles, the rate in the upper beam was about 7 % larger than in the lower beam. Let us write n and N for the number of kaons in the absorbed and the monitoring beams. We thus define two attenuations $a_H = N_L/n_H$ and $a_L = N_H/n_L$ labeled according to the beam in which the absorber is. Similarly, the attenuation used to calculate the total cross-section is $a = (N_H + N_L)/(n_H + n_L)$. In order to exhibit rate effects, we thus plot in Fig. 6.3 the ratio a_H/a_L and in Fig 6.4 a exp(L/X) as a function of the beam intensity: both quantities should be equal to 1 and independent of the rate. To obtain these plots we used the fact that, because of the accelerator running conditions and problems, the data runs were actually taken with varying intensities on the primary target as measured by the SEM. In Fig. 6.3 we see clearly a correlation with the beam intensity, while the correct attenuation in Fig. 6.4 does not show any rate dependence.

6.3. Corrections to the total cross-section

The extrapolation to zero angle with formula (2.5) requires knowledge of the elastic scattering parameters for K_L on nuclei. They were estimated by the Glauber model, and for instance the K_L elastic diffraction logarithmic slope was found to be closely approximated by $b \simeq 10 \ A^{2/3}$ $(GeV/c)^{-2}$. The solid angle, $d\Omega \simeq 6.4 \times 10^{-9}$ strad, was calculated from the measured aperture of the collimators. The setting of these collimators was kept the same for all the data runs, including regeneration measurements.

The correction for scattering from one beam into the other one was determined by a special Monte Carlo program. It used the exact longitudinal and transverse positions of the collimators, and allowed

for multiple scattering through the lead radiator, the slabs and
the collimators. Fig. 6.5 shows the calculated probability of a kaon
to scatter from one beam into the other as a function of its momentum,
under normal running conditions (i.e. 7.5 cm of Pb radiator). One
sees from the figure that the momentum dependence can be approximated
as

$$c = 3.8 \ 10^{-6} \ p^{1.47} \tag{6.1}$$

In Fig. 6.6 we show a measurement of this probability as a function
of the Pb radiator thickness. This figure clearly demonstrates the
correlation between the thickness of the Pb radiator (which acts as
a kind of secondary target) and the amount of scattered events . The
intercept at zero corresponds roughly to the probability of a kaon to
leak through 1.22 m of steel ($\cong 5 \ 10^{-4}$). The average beam momentum
being 65 GeV/c, the measured scattering probability for 7.5 cm of Pb,
$(2.0\pm0.2) \ 10^{-3}$, is in good agreement with the Monte Carlo calculation.

Thus, the complete correction to the number of transmitted kaons,
given by formula (2.7), was

$$N_\pi = N_\pi^{obs} / \left(1 + d \ p^2 + c \right) \tag{6.2}$$

were c is calculated with (6.1) and d is found in table 6.2 for the
corresponding target. We estimate that the accuracy of this correction
is of the order of 20 %.

6.4. Total cross-section results

In table 6.3 we give the results for the total cross-section measured
with unambiguous Kµ3 's. The unambiguous cut, $|ARG| < .01$, insures that
the uncertainty on the momentum of the kaon ($\pm$ 10 %) is compatible

with the binning of the data (10 GeV/c). But, as this unambiguous cut discards about 57 % of the total number of Kμ3's, it is worth trying to find a method to use all of them.

In our momentum range, the total cross-section is almost constant with momentum. This is clearly shown by the smallness of the slope coefficient of linear fits to the data in the form

$$\sigma_T = A + B\, p \qquad (6.3)$$

given in Table 8.1. Thus, to first approximation, the momentum spectrum of the attenuated and the monitoring beams are the same. Therefore, we can use a weighting technique to use not just the unambiguous Kμ3 decays, but all of them.

Let S(p) be the momentum spectrum of the kaons detected by our apparatus as obtained from the unambiguous Kμ3 sample. For the determination of S(p), the decays in the monitoring beam from all the targets can be added together. Therefore this momentum spectrum can be considered, in principle, as "exactly known". To the two solutions of the Kμ3 kinematics we give the following weights :

$$W_1(p_1) = \frac{S(p_1)}{S(p_1) + S(p_2)} \qquad W_2(p_2) = \frac{S(p_2)}{S(p_1) + S(p_2)} \qquad (6.4)$$

and both solutions are entered with the corresponding weights in their respective momentum bins.

The total cross-section calculated with "all" the Kμ3's are given in table 6.4.

The systematic errors on the "unambigous" method come from uncertainties on the target parameters (Table 3.1) and on the corrections (6.2). The resulting systematic error is thus of the order of 0.5 to 1% .

Although the "all" Kμ3 method is simple in itself, the systematic error in it is in practice very difficult to calculate. Also, the method is, in principle, only correct to the limit of a total cross-section constant with momentum. We thus prefer to obtain an estimate of this systematic error by comparing the results of the two methods. Comparing the results of the fits to (6.3) for both methods, we see that they agree within better than 1 % for all targets.

Finally, an independent investigation of possible systematics was provided by the special "half-length" Sn target. This second measurement of the Sn total cross-section (in different rate and background conditions) is readily seen to be compatible with the first one. Comparing the results of the fits to (6.3), we see that the results for the two target lengths, with both "unambiguous" and "all" Kμ3 methods, are consistent to better than 0.5 %.

6.5. Regeneration data

Regeneration on hydrogen[14] and carbon[5] having been measured in the same beam line previously, in this experiment we measured coherent K_S regeneration on the heavier targets Al, Cu, Sn and Pb. The number of triggers, reconstructed events and events after cuts for these targets are given in Table 6.5. The Kμ3 triggers were prescaled by a factor of 2 or 4 as indicated in the same table.

A special run was taken in order to obtain an independent measurement of the CP violating amplitude η_{+-}. Instead of having an absorber in one beam and a regenerator in the other one, as for the regeneration measurements, the absorber was removed to yield more "vacuum" Kπ2's. Also the thin shower counter was put in anti-coincidence in the trigger to remove as many as possible Ke3's at the trigger level already. For this run, labeled "η_{+-}" in Table 6.5, the Kμ3's were prescaled by a factor of 8.

6.6 Regeneration results

The regeneration amplitude is readily obtained from the data using the
method described in paragraph 2.2, after having corrected the $K\mu3$'s
according to (6.2) and (5.13), giving the results listed in Table 6.6.
The various physical parameters used in the calculation are given in
Table 6.7. We took the Particle Data Group values[10], except for $|\eta_{+-}|$,
   for which we used the average of all the published measurements
compiled in[10], plus several more recent results[15], giving

$$|\eta_{+-}| = (2.183 \pm 0.023) \times 10^{-3} \qquad (6.5)$$

6.7. Systematics in regeneration

The determination of the regeneration amplitude requires the precise know-
ledge of the ratio $A(K\pi2,p)/A(K\mu3,p)$ of the acceptances. Mistakes in the
M.C. would therefore result in a systematical error. As the momentum-
dependence of this ratio is a rather smooth function of momentum, we
expect that the numerous checks made are sufficient to insure that this
dependence is properly understood. But, the correctness of the relative
normalization provided by the M.C. is much more difficult to ascertain.
We will therefore concentrate on these systematics affecting the
normalization of the result.

There are 3 main sources contributing to the systematics in the re -
generation results :

(1) Uncertainties in the target parameters (Table 3.1) and in the
physical constants (Table 6.7).

(2) Uncertainties in the $K\mu3$ normalization.

(3) Uncertainties in the $K\pi2$ background substraction.

As the first contribution is obvious, we will now examine the systematics in the Kμ3 normalization. Firstly, there is the problem of the muon identification. To study this procedure consisting of determining which of the two tracks in a Kμ3 decay is the muon, we applied very severe cuts on the Kμ3 data, i.e. we rejected all the events with more than 1 counter (or 1 adjacent pair of overlapping counters) hit in C5. On genuine muons, as recorded in the special single track muon runs, this cut removed 5.7 % of the tagged events. Applying this cut to the Monte Carlo as well (to take care of pion decay in flight), and correcting for the 5.7 % measured loss, we recalculated $\left| \frac{f - \bar{f}}{p} \right|$ to find the same answer within 0.5 %. This test insures that they are essentially no accidentals in C5, and that the multiple hits in that counter are understood in terms of delta rays.

Secondly, there is a possible systematics in the Kμ3 normalization to come from the "unambiguous" cut. But as 43.2 % of the data events are accepted by this cut, and 43.7 % of the M.C. events, we estimate this systematic uncertainty to be less than 0.5 % .

To proceed with the systematics in the Kπ2 background substraction, we recall that there are 3 main contributions to the background under the coherent peak in the p_t^2 distribution :

(1) Diffracted K_S's, which have a p_t^2 dependence in exp $(-bp_t^2)$ with $b \simeq 13\ A^{2/3}$ $(GeV/c)^{-2}$.

(2) Ke3's with pion decay in flight.

(3) K_S's inelastically produced in the target.

The two latter contribution have a p_t^2 dependence that can be considered as flat in our momentum transfer range, $\Delta p_t^2 = 1000\ (MeV/c)^2$.
Our background substraction formula (5.12), is assuming the background to be

essentially flat. Ke3's and inelastic K_S's are thus taken care of, but we underestimate the diffractive background by the factor

$$1 - \exp(-\tfrac{1}{2}b \, \Delta p_t^2) \tag{6.6}$$

which is about 20 % for Pb. To evaluate the relative importance of this bias, we need to know the ratio of the number of coherent K_S's over the number of diffracted K_S's in the momentum transfer interval Δp_t^2. This so-called "Good ratio", is a property of the regenerator it-self, independent of the regeneration amplitude. For a thin regenerator the Good ratio takes the simple form[16]

$$R = N_{coh}/N_{diffr} = 4\pi NL/\Delta p_t^2 \tag{6.7}$$

which gives about 8, 13, 22 and 53 for our respective Pb, Sn, Cu and Al regenerators. But, for thick regenerators, multiple scattering corrections are increasing R to a value which (for two interaction length regenerators), is about 3 times larger as given by (6.7). In the case of Pb, which is the worse, we have thus $R > 20$ and the error on the number of coherent $K\pi 2$'s (implied by our flat background assumption) is of the order of 1 %. The resulting systematical uncertainty on the Pb regeneration is therefore around 0.5 %, and becomes, for the lightest targets, much smaller.

In Table 6.6, the statistical errors quoted include the contributions from the acceptances (Table 5.1). We estimate the total systematic error (resulting from uncertainties in the physical parameters, systematics in the cutting, the background substraction procedures and the acceptances calculation with the Monte Carlo, to be of the order of 2% to 3%.

6.8. $|\eta_{+-}|$ determination.

An indication of the systematics in both Kμ3 normalization and Ke3 background substraction in Kπ2 is provided by the measurement of the CP violation parameter $|\eta_{+-}|$. Adding together the "vacuum" Kπ2 and Kμ3 decays in the monitoring beam for our 4 targets, we get from formula (2.17) $|\eta_{+-}| = (2.15\pm0.05) \times 10^{-3}$. Considering that with our standard cuts the signal (Kπ2) to noise (Ke3) ratio is only of about 1 to 4, the result is in reasonable agreement with the world average (6.5). By tightening the cuts on the Kπ2's, one could somehow improve the above signal to noise ratio, but it is not worth while as a much better Ke3 rejection can be obtained by employing the shower counters. To do so, we took a special run optimized in order to get a good determination of $|\eta_{+-}|$. As already described in 6.5, we recorded Kπ2 decays with the thin shower counter in anti-coincidence in the trigger.

The number of Kπ2 decays in the vacuum beam (no absorber and no regenerator) is given by (2.15, 2.8) with L=0, i.e.

$$N_V(K\pi2,p) = N_I \, BR(K\pi2) \, A(K\pi2,p) \, |\eta_{+-}|^2 \, \Gamma_S \int_{\tau_1}^{\tau_2} e^{-\Gamma_I \tau} \, d\tau \qquad (6.8)$$

while the number of Kπ2 decays behind the regenerator in the other beam is still given by (2.8). In this measurement the regenerator acts as a converter, monitoring the incident K$_L$ flux we can obtain with our measured results of ρ and of the total cross-section. We thus get from (6.8) and (2.8) an equation for $|\eta_{+-}|$. With our standard cuts we find

$$|\eta_{+-}| = (2.186\pm0.029) \times 10^{-3}$$

As this method makes direct use of only Kπ2's in either beam, we can apply very tight shower counter cuts to reduce even more strongly the Ke3 background. We obtain finally

$$|\eta_{+-}| = (2.20\pm0.045) \times 10^{-3} \qquad (6.9)$$

where the error includes the statistical errors and the errors on the external parameters.

The consistency of our two independent determinations of $|\eta_{+-}|$, their stability under various cuts, and their good agreement with the world average, are positive indications of the validity of our methods.

7.   GLAUBER MODEL OF K_L NUCLEUS INTERACTIONS

The Glauber model[3] highly successfully describes elastic hadron-nucleus interactions up to energies of a few GeV. At higher energies, it has been since long anticipated that the inelastic intermediate states (IIS) would spoil this agreement[17]. Measurements of neutron-nucleus total cross-sections at Fermilab[2] have in fact shown that a significant correction of about 5 % has to be applied to the Glauber prediction in order to secure agreement with the data. This inelastic shadow correction is due to the rescattering of beam particles excited within nucleus. An excited hadron can, in a subsequent collision, be converted back into its ground state before leaving the nucleus ; such an effect increases the mean free path within the nucleus. It is thus intuitively obvious that the total cross-section on the nucleus will as a result decrease, whereas production precesses like coherent regeneration will increase.

Using a coupled channel optical model, Karmanov and Kondratyuk [4] have estimated the magnitude of this inelastic shadowing in heavy nuclei. Their first assumption is to keep only the first-order inelastic process where, in the multiple scattering chain, the projectile gets excited only once and scatters normally before returning into its ground state (see Fig. 7.1).

Of course, this assumption neglects the more complicated diagrams in which the projectile gets excited several times. But, as the effect of IIS is at most of the order of 10 %, one may safely ignore those processes contributing at the 1 % level only.

Their second assumption is to take for the excited states the same scattering properties as for the beam particle. This hypothesis can be best understood in the space-time picture of strong interactions : The formation time of an inelastic state of mass M takes a finite time on the order of the inverse pion mass (i.e. about 1 fermi). The corresponding formation length in the laboratory is hence $L \simeq (E/m)(1/m_\pi)$,

where E/m is the Lorentz dilatation factor, and is at high energies much larger than the nuclear radius[18]. In the parton language this means that the wee parton which interacts with a target nucleon does not "know" into which state the incoming particle will finally transform. Thus it is expected that the scattering properties of the inelastic state within the nucleus will not differ too much from those of the ground state. This prediction has recently been verified for diffractively produced inelastic states at Fermilab by studying diffractive dissociation on deuterium[19].

Their third assumption is to connect the production (absorption) amplitude of the inelastic intermediate states to the diffractive dissociation of the projectile. This assumption is thoroughly discussed by Kaidalov and Kondratyuk[20] with much attention given to the non-diffractive inelastic background. Also, it is obvious that the excitation and the desexcitation of the projectile within the nucleus are, in some sense, time-reversed processes. Therefore, setting spin and isospin complications aside, their respective amplitudes are simply complex conjugates if only vacuum quantum numbers are exchanged. In fact, for a pure Regge-pole exchange

$$ f\left(N^{*} \rightarrow N \right) = \zeta\, e^{-i\pi\alpha(t)}\, \bar{f}\left(N \rightarrow N^{*} \right) \tag{7.1} $$

where ζ is the signature and $\alpha(t)$ the trajectory function. A pomeron with $\alpha(0)=1$ gives the desired result. Assuming that the main contribution to the inelastic intermediate states at high energy comes indeed from diffractive dissociation, the inelastic screening correction will be proportional to

$$ f\bar{f} = |f|^{2} = \frac{p^{2}}{\pi}\frac{d\sigma}{dt} \tag{7.2} $$

where the differential cross-section corresponds to the inclusive reaction

$$K + N \longrightarrow X + N$$

We will parametrize this reaction as

$$\frac{d\sigma}{dt} = \int dM^2 \frac{d^2\sigma}{dt\,dM^2} = \int dM^2 \frac{d^2\sigma}{dt\,dM^2}(t=0)\,\exp(\gamma t) \qquad (7.3)$$

and take, in agreement with the second assumption, γ equal to the elastic slope parameter.

Maintaining the three basic assumptions of Karmanov and Kondratyuk, we have rederived their result in the framework of the Glauber model. We obtain a more complete formula, valid for all nuclei (even as light as deuterium), which includes the effect of the inelastic states on the real part of the hadron-nucleus amplitude. Our model takes also the t-distribution of the diffractive dissociation into account. (For the details of the derivation see appendix A). The complete formulae used in our model are the following :

We take for the nuclear density the usual spherically symetric distributions, i.e. for heavy nuclei ($A > 27$) the Woods-Saxon distribution :

$$\rho(r) = \left[\frac{4}{3}\pi R^3 \left(1 + \left(\frac{\pi s}{R}\right)^2\right)\left(1 + \exp\left(\frac{r-R}{s}\right)\right)\right]^{-1} \qquad , \qquad (7.4)$$

for light nuclei ($27 > A > 2$) the harmonic oscillator distribution :

$$\rho(r) = \frac{4}{A}\left(\frac{c^2}{\pi}\right)^{3/2}\left[1 + \left(\frac{A}{6} - \frac{2}{3}\right)c^2 r^2\right]\exp\left(-c^2 r^2\right) \qquad , \qquad (7.5)$$

and for deuterium the gaussian distribution :

$$\rho(r) = \left(\pi G^2\right)^{-3/2}\exp\left(-r^2/G^2\right) . \qquad (7.6)$$

The classical Glauber-Franco formula for the forward elastic scattering amplitude at $q^2=0$ reads[21]

$$f^G(0) = \frac{ip}{2\pi} \int d^2b \left[1 - \left(1 - \Xi_p(b)\right)^Z \left(1 - \Xi_n(b)\right)^N \right] \qquad (7.7)$$

where Ξ_p and Ξ_n are the nuclear-averaged profile functions on the target proton and neutrons :

$$\Xi_{p,n}(b) = \frac{4\pi}{p} \int_0^\infty dq\, J_0(qb)\, f_{p,n}(q^2) \int_0^\infty dr\, r\, \rho_{p,n}(r) \sin(qr) \qquad (7.8)$$

The elementary elastic scattering amplitude $f_{p,n}(q^2)$, which has to be fed in for both K^0 and $\bar{K}^0$ on proton and neutrons, is parametrized as

$$f_{p,n}(q^2) = \frac{p}{4\pi}(i+a)\sigma \exp\left(-\beta q^2/2 + \delta q^4/2\right) \qquad (7.9)$$

As usual, σ is the relevant kaon-nucleon total cross-section, a the ratio of real to imaginary parts of the amplitude and β, δ the q^2-dependence coefficients.

The inelastic screening correction to this nuclear elastic amplitude reads

$$f^*(0) = -2ip\, A(A-1) \int d^2b \left[1 - \Xi\right]^{A-2} \int_{(m+m_\pi)^2}^{(\sqrt{s}-m)^2} dM^2\, \frac{d^2\sigma}{dt\, dM^2}(t=0)\, \Phi(Q,b)$$

In this expression we do not distinguish the protons and the neutrons of the target. We take therefore an average nucleon profile function defined by

$$(1 - \Xi)^A \equiv (1 - \Xi_p)^Z (1 - \Xi_n)^N \qquad (7.11)$$

For the inelastic formfactor we find

$$\Phi(Q,b) = \frac{1}{2}(2\pi\alpha^2)^{-2} \exp(-b^2/2e^2 - Q^2\alpha^2)[1 - erf(iQ\alpha)] \quad (7.12)$$

with

$$\alpha^2 = \frac{1}{2}(G^2 + 2\gamma)$$

and

$$Q = \frac{M^2 - m^2}{2p} \quad (7.13)$$

This explicit formula is obtained by using a Gaussian nuclear density for the nucleus in the calculation of the inelastic screening. This unessential approximation is made in order to reduce the number of numerical integrations that would be needed otherwise. The radius of this gaussian is taken so to match the RMS radius of the nucleus, i.e. :

$$G^2 = \frac{3}{2}\langle r^2 \rangle \quad (7.14)$$

Q, defined by (7.13), is the minimum longitudinal momentum transfered in the production of the inelastic intermediate state of mass M. Finally, because of the numerous approximations made, the accuracy of this inelastic screening correction formula will be, at best, of the order of 10 %. Considering the serious uncertainties in the current knowledge of diffractive dissociation, this accuracy seems adequate.

Now one has to mention that in principle there is a correction arising from the interaction of the neutral kaons with the electrons of the target. This interaction is due to the finite K^0 charge radius which is one consequence of the compositeness of the kaon. The strange quark being heavier than the down quark, one expects the K^0 electro-magnetic form factor to be negative, while the $\bar{K}^0$ form factor will have the opposite sign. The K^0 electron scattering amplitude is purely real and in the forward direction equal to[22]

$$f^e(0) = (-Z)\left(-\langle v_K^2\rangle\right)\frac{\alpha}{3}\, p \tag{7.15}$$

where $\langle v_K^2\rangle$ stands for the absolute value of the squared K^0 charge radius, and α is the fine structure constant. But, the elementary particle cross-sections from which we obtain the amplitudes (7.9) are the strong interaction cross-sections, i.e. corrected for electro-magnetic effects. Thus, assuming negligible electro-magnetic screening, the charge of the nucleus is essentially canceling the effect of the electrons in the forward direction. As in any case, with optimistic model predictions of the neutral kaon form factor[23], the contribution from the electrons alone calculated with formula (7.15) would result in a less than 2 % corrections to the regeneration amplitude on Pb at 100 GeV/c, we can safely neglect this effect.

Finally, combining the Glauber and IIS contributions, the <u>total forward scattering amplitudes</u> will be

$$f(0) = f^G(0) + f^{\%}(0)$$
$$\bar{f}(0) = \bar{f}^G(0) + \bar{f}^{\%}(0) \tag{7.16}$$

We can now calculate the total cross-section

$$\sigma_T\left(K_L + A \longrightarrow K_L + A\right) = \frac{4\pi}{p}\frac{1}{2}\left[f(0) + \bar{f}(0)\right] \tag{7.17}$$

and regeneration amplitude

$$\tilde{\rho}\left(K_L + A \longrightarrow K_S + A\right) = \frac{1}{p}\left[f(0) - \bar{f}(0)\right] \tag{7.18}$$

where in (7.16) to (7.18) the "$^-$" sign refers to the $\bar{K}^0$.

8. INTERPRETATION OF THE DATA

8.1 The results

In Fig. 8.1 and Fig. 8.2 we present our total cross-section and regeneration results, together with all other, i.e. lower energy, data known to us. On these graphs we have drawn the curves of interpolation fits to the data in our momentum range, i.e. 30 to 130 GeV/c. For the total cross-section we used the form

$$\sigma_T = A + B\rho \qquad (8.1)$$

and for regeneration

$$|(f-\bar{f})/\rho| = \Upsilon \, \rho^{\alpha-1} \qquad (8.2)$$

The parameters resulting from these fits are given in Table 8.1.

Looking first at the total cross-sections data, we see from both Fig. 8.1. and the slopes of the fits that the momentum dependence changes sign from the lightest to the heaviest targets. While the total cross-sections for the light nuclei are essentially constant, the total cross-section for Pb is clearly decreasing as a function of the momentum. As the kaon-nucleon total cross-sections are well known to be rising above 50 GeV/c, this behaviour suggests the need for some correction such as inelastic screening.

In Fig. 8.2, the available low energy regeneration data has been scaled for $|\eta_{+-}|=2.183\times10^{-3}$ wherever the "interference method" had been used in the original analysis. For carbon, it is known that the regeneration amplitude is dominated by the exchange of a single Regge-trajectory, the ω,[5]. A single power-law fit (8.2) to the FNAL data extrapolates nicely to the low energy points at a few GeV, a spectacular confirmation of Regge phenomenology. For Pb, however, while the power-law exponent in our momentum range is compatible with that for C, the single power-law does not extrapolate

down to the few GeV region: the data show a change in slope. In Fig. 8.2
we have also included preliminary Pb regeneration data obtained in the
same beam as a by-product of an experiment aimed at the measurement of the
K^O form factor[34]. These data are in good agreement with ours, thus con-
firming the change in slope. The experiment also provides a measurement of
the _phase_ of the regeneration amplitude for Pb, yielding arg $(f-\bar{f})$ = $-(124\pm2)^O$
when constrained to a constant value in the 35 - 115 GeV/c range.

We now want to compare these results with the Glauber model of hadron-
nucleus interactions. To do so we will take the most "natural" approach, i.e.

(i) calculate the nuclear scattering amplitude $f(0)$, $\bar{f}(0)$ with the standard
Glauber model (no IIS) assuming the nuclear matter density distribution to
be _identical_ to the charge distrubution as measured by electron scattering
and mesic atom transitions;

(ii) attribute the discrepancy between this prediction of the total cross-
section, $4\pi/p \ Im(f+\bar{f})$, and the data to the contribution of inelastic screening;

(iii) predict the nuclear regeneration amplitude, $(f-\bar{f})/p$, assuming the amount
of inelastic screening to scale with the respective elementary total cross-
sections;

(iv) interpret any residual discrepancy between this prediction of regeneration
and the data as possible insufficiencies of the model.

In Fig. 8.3 we summarize in an organigram the details of this program.

We shall now start by the parametrization of the inputs of the model, i.e.

- The forward elastic scattering amplitude of the $K^O p$, $K^O n$, $\bar{K}^O p$, $\bar{K}^O n$
channels.

- The inclusive forward diffractive dissociation differential cross-sections
$d^2\sigma(K^O)/dtdM^2$ and $d^2\sigma(\bar{K}^O)/dtdM^2$.

- The proton and neutron nuclear density distributions

$$\rho_n = \rho_p = \rho(r, A, Z)$$

8.2. Forward scattering amplitude parametrization

From isospin invariance of strong interaction the neutral kaon amplitudes
are obtained from the corresponding charged kaon amplitudes:

$$f(K^0 p) = f(K^+ n)$$

$$f(K^0 n) = f(K^+ p)$$

$$f(\bar{K}^0 p) = f(K^- n)$$ \qquad (8.4)

$$f(\bar{K}^0 n) = f(K^- p)$$

For calculating only the nuclear total cross-sections by the Glauber model
the direct use of the measured charged kaon total cross-sections and real
parts would be sufficient. For the prediction of the regeneration amplitude,
which involves the difference of two relatively large amplitudes, one has
first to smooth out the input data to eliminate the experimental point-to-
point fluctuations. The modulus of the regeneration amplitude also requires
a precise knowledge of the real part of the forward amplitude, which at
high energies is poorly known. We thus had to rely on a Regge model and
dispersion relations to parametrize the kaon-nucleon amplitudes. The
complete formulae used are given in appendix B. We assumed strong exchange
degeneracy of the (ρ, A_2) and (ω, f) trajectories, and a $\log^2(p)$ increase
of the Pomeron trajectory with momentum.

The main problem encountered in fitting the (K,N) cross-sections with our
Regge model is that the ω intercept $\alpha_\omega(0)$ was found to be equal to 0.44 ± 0.01
(in agreement with other standard phenomenological analyses, i.e.[6]), while
the same intercept inferred by the power law dependence of regeneration in
carbon is 0.397 ± 0.003 [5].

In order to find out about this discrepancy, we shall compare the results of the Glauber model with the data, using as inputs the amplitudes obtained by constraining $\alpha_\omega(0)$ to either its "elementary" value (i.e. 0.44), or to its value coming from carbon regeneration (i.e.0.40).

Appendix B describes these fits and gives the resulting parameters (Table 8.2), as well as the parametrization of the elastic slope coefficients (7.9). In Table 8.3 we list for a few energies the fitted total cross-sections and real to imaginary parts ratios calculated with these parameters. Predictions of regeneration on hydrogen and charge exchange reactions included in this table are in excellent agreement with the data.

8.3. Diffractive dissociation parametrization

The differential cross-section for the diffractive production on nucleon of states with mass M^2 is poorly known for kaons. Nevertheless, one expects theoretically that diffractive processes are scaling with the total cross-section, i.e.

$$\frac{\frac{d^2\sigma}{dt\,dM^2}(aN \to a^*N)}{\sigma_T(aN \to aN)} \simeq \frac{\frac{d^2\sigma}{dt\,dM^2}(bN \to b^*N)}{\sigma_T(bN \to bN)} \tag{8.5}$$

Clearly, at low M, this is only an approximation as the quantum numbers for different projectiles are not the same. For instance, with protons one expects Δ^* resonances, and for kaons Q like bumps in the low missing mass region ($M^2 \lesssim 10$ GeV^2). But, in the high excitation mass region, the so-called "triple-pomeron" coupling term is expected to dominate[35]. The calculation of the IIS contribution with formula (7.10), involves an integration over M^2. Thus, in fact, to first order only the "sum rule" implied by integrating (8.5) on both sides is required to be valid for our estimation of the inelastic screening to be correct.

Consequently, we will take for $d^2\sigma/dtdM^2$ a fit to the proton diffractive dissociation $pp \rightarrow pX$ given by Murthy et al[2], and scale if for K^0, $\bar{K}^0$ according to the law (8.5). The explicit form is

$$d^2\sigma/dtdM^2(t=0,M^2) =$$

$$(M^2 <5) \qquad = 26.47\mu -35.97\mu^2+18.47\mu^3-4.14\mu^4+0.345\mu^5$$

$$(M^2 >5) \qquad = 4.4/M^2 \qquad\qquad (8.6)$$

where $\mu= M^2 - 1.17$.

Finally, we recall that the IIS correction is a 10% effect at most, and that our treatment of it is only an approximative one. At this level of precision it turns out that the scaling relation (8.5) and the associated sum rules are certainly adequate.

8.4. Nuclear matter density distribution parametrization

In the Glauber model, the relative size of the projectile in its interaction with the nucleons is given by the t dependence of the forward scattering amplitude. Thus the matter distributions to be used for the nucleus have to be taken as measured by point-like projectiles. The proton distribution must therefore be taken identical to the charge distribution, but there are no such direct measurements possible for the neutron distribution.However (because of charge independence of strong interactions), for light nuclei and especially for I=0 nuclei the neutron distribution must be essentially equal to the proton distribution. The only uncertainty left in the parametrization of the neutron distribution is thus for heavy nuclei. For such neutronrich nuclei, some nuclear shell models predict neutron RMS radii 0.2 to 0.3 fm larger than the corresponding proton RMS radii[36]. This is in contradiction with several recent experiments, i.e. 1 GeV proton-nucleus scattering interpreted with the Glauber model, which

have consistently shown that this difference was in fact compatible
with 0, or at most of 0.05 to 0.1 fm[37]. We shall therefore take for
the nuclear matter distribution the charge distribution measured in
electron scattering experiments. The parameters, taken from the
compilation[38], are given in Table 8.3.

As it is well known[39], the prediction of total cross-section by the
Glauber model depends essentially only on the RMS radii of the nucleus.
The mean radius and the skin thickness have, for a given RMS, only second
order effects, affecting mostly the structure of the diffraction pattern.
On the other hand the regeneration amplitude is much more sensitive to
the nuclear surface[40]. For instance, a variation of 0.1 fm in the neutron
skin thickness parameter S in (7.4) for a given RMS radius produces a
0.1% change in the total cross-section for Pb, whereas the regeneration
amplitude modulus changes by about 0.6%. Similarly, for a given skin
thickness, a change of 0.1 fm, in the RMS radius of the neutron distri-
bution alone produces a 0.7% change in the Pb total cross-section, whereas
the regeneration amplitude modulus changes by 2%.

Although this sensitivity to the neutron distribution is quite substantial,
we will not (because of IIS and uncertainties in $|\eta_{+-}|$) be able to actually
"measure" the neutron distribution parameters in the heavy nuclei. However
we will be clearly in position to see wether the neutron and proton
distributions are compatible within a few 0.1 fm or not.

8.5. Neutron-nucleus total cross-sections

The precise neutron-nucleus data Murthy et al.[2] were the first to
clearly reveal the inelastic screening effects at FNAL energies.
Comparing their results to rather old measurements of the nuclear charge
radii, Murthy et al. concluded that nuclear matter distributions
different from the electron scattering results were required (see also[41]);
Their data are in fact in excellent agreement with more recent measurements
of the electromagnetic radii.

Using the fits to the neutron-nucleon cross-section described in appendix B, and summarized in table 8.2, we obtain the predictions of the (n, Cu) and (n, Pb) total cross-section shown in Fig. 8.4. One sees that our more complete treatment of the IIS produces some anti-shadowing at low momenta, thus improving the agreement between the model and the data. (A more complete model of IIS would introduce, aside from the diffractive states, N^* contributions that would also produce antishadowing at low momenta[42]).

To show how well the A-dependence of the IIS is predicted, we plot in Fig. 8.5 the discrepancy between the standard Glauber model (without IIS), and the measured total cross-sections at 200 GeV/c for all nuclei studied by Murthy et al. The accuracy of the inelastic screening prediction (with the same parametrization of the diffractive dissociation as Murthy et al.) is quite remarkable.

8.6. Kaon-nucleus total cross-sections

In Fig. 8.6 we present the prediction of the kaon-nucleus total cross-sections. The lack of data in the low-energy region does not allow a detailed comparison of the momentum dependence of the total cross-section as it was possible for the neutron-nuclei data. Nevertheless, the agreement is seen to be very good and thus the scaling rule (8.5) is found to be valid without any adjustment.

Specifically we took

$$\frac{d^2\sigma}{dt\,d\eta^2}(K^0 N \to XN) = \frac{\sigma_T(K^0, N)}{\sigma_T(p, N)} \frac{d^2\sigma}{dt\,d\eta^2}(pN \to XN) \tag{8.7}$$

$$\frac{d^2\sigma}{dt\,d\eta^2}(\bar{K}^0 N \to XN) = \frac{\sigma_T(\bar{K}^0, N)}{\sigma_T(p, N)} \frac{d^2\sigma}{dt\,d\eta^2}(pN \to XN)$$

The A-dependence of the inelastic screening correction at 50 GeV/c
is shown in Fig. 8.7. The agreement is excellent again, except may
be for carbon.

An interesting display of the A-dependence of the IIS is obtained
by plotting the relative correction of neutron and kaon total cross-
section on the same graph, Fig. 8.8. Because of the larger mean free
path of kaons inside the nucleus, the IIS contribution is in heavy
nuclei larger for kaons than for neutrons. The IIS correction for
kaons has also a maximum for $A \simeq 120$.

The IIS contribution measured on heavy nuclei, extrapolated down to
A=2 by the model, gives a very precise self-consistent prediction of the
inelastic shadow correction for the deuteron. This can of course have
very useful applications for extracting total cross-sections on neutrons
from deuteron data.

8.7. K_S regeneration

The success of the Glauber model with IIS for the total cross-section
permits a univocal prediction of the regeneration amplitude, provided
the scaling assumption (8.5) and the ω intercept are correct. The first
condition is necessary because the IIS correction on the total cross-
section corresponds to the sum of the K^o, $\bar{K}^o$ amplitudes, while for the
regeneration one needs the IIS correction to their difference. Thus
the relation (8.5) provides the link allowing the IIS correction
to regeneration to be self-consistently constrained by the total cross-
section measurements. The second condition is important because a variation
of 0.01 in the ω intercept results at 100 GeV/c (as $100^{0.01} = 1.05$) in a
5% difference in the prediction !

In Fig. 8.9 we compare the Glauber model prediction with IIS to the data taking $\alpha_\omega(0)=0.44$ as given by standard Regge fits. (We recall that this value of $\alpha_\omega(0)$ gives a good agreement with the preliminary results for regeneration from Hydrogen[14]). The prediction disagrees with the data by 10 to 20% at all momenta, and for all nuclei. In heavy nuclei, the IIS contribution merely increases the disagreement.

In Fig. 8.10 we compare the data with the Glauber model including IIS, taking $\alpha_\omega(0)=0.397$(as obtained from regeneration on carbon). The agreement is excellent at all momenta and one sees that the IIS correction is essential to secure agreement at high energy for the heavy nuclei.

An other feature of the data from heavy nuclei, i.e. the change in slope when going from low to high energies, is also predicted correctly. This effect is simply a consequence of the rise of the total cross-sections with energy. For instance, keeping only the first two terms of the Glauber series, one has approximately

$$\frac{F-\bar{F}}{P} \simeq A\left(\frac{f-\bar{f}}{P}\right)\left(1 + i\varepsilon\,(A-1)\frac{f+\bar{f}}{P}\right) \tag{8.8}$$

where ξ is a function of the nuclear density. Thus, if the elementary kaon-nucleon total cross-sections increase with energies, the Glauber shadow correction becomes larger at high momentum[43]. Because of the (A-1) factor in (8.8), this effect is too small to be observed in light nuclei.

When comparing the nuclear phase (i.e. $-132°$) predicted by our model for Pb, with the phase measured in the neutral kaon form factor experiment[34], the agreement is less good. But, as the phase in our model was $-126°$ before taking the IIS correction into account, it is possible that our oversimplified model of IIS cannot predict the phases accurately.

We thus conclude that, in Regge phenomenology, the scattering on nuclear targets can be interpreted self-consistently by taking for the ω-trajectory an _effective intercept_ that differs from the one measured with elementary targets. Furthermore, the magnitude of the IIS correction required by the data is properly predicted by our model.

8.8 Criticism of the model and input parameter dependence

In the previous paragraph, we have seen that the data can be interpreted quite naturally. For instance, we find it unnecessary to introduce

(i) Different nuclear matter distributions for proton and neutron.

(ii) Special shadowing or antishadowing effects such as "pionisation"[44] that could partly cancel the effects of diffractive intermediate states.

(iii) Complex nuclear effects in which "space-time" effects and "ladder graph" contributions[45] would totaly invalidate the use of the Glauber model.

The only "new" concept we had to introduce is possibly that of an "effective" $\alpha_{\omega}(0)$ in nuclear matter.

To make these conclusions more quantitative, we have to evaluate the "precision" of our model. Because of the number of approximations made, especialy in the IIS prediction, this task is quite a difficult one. We thus content ourselves of calculating the effects of typical input parameter variations on the predictions at 10 and 100 GeV/c (Table 8.5). As an exemple, from this table we see that a 10% increase in neutron RMS radius in Pb [46] would imply a 20% increase in the re-generation amplitude prediction. This would put the prediction in clear contradiction with the data. As the regeneration amplitude is known to come mostly from neutrons, this is a strong indication of the correctness of conclusion (i) above.

8.9. Conclusion

The general success of the Glauber-Regge phenomenology found in interpreting the data of this experiment shows that low momentum transfer interactions on nuclei at high energies are to a high degree of precision explained by standard concepts. The main conclusions that may be drawn from this success are:

(i) For the nuclear physicist, that the RMS radii of the nuclear matter density distributions of protons and neutrons are equal to within a few percent.

(ii) For the theoretician, that the Glauber and Karmanov-Kondratyuk models are adequate to describe the data up to 150 GeV/c.

(iii) For the Regge phenomenologist, that the hadron-nucleus interactions at high energies can be self-consistently interpreted in terms of an "effective" ω intercept, substantially different from the "elementary" ω intercept.

A. GLAUBER MODEL WITH INELASTIC INTERMEDIATE STATES

A.1. Coherent processes at high energy. Transverse and longitudinal coordinates

The coherent processes we shall describe with the Glauber model are reactions of the type

$$B + A \longrightarrow X + A'$$ (A1)

where B is the beam particle of mass $m_B = m$ and A, A', is the target nucleus. X is the produced system of mass $m_X = M$ (may be equal to B, i.e. m=M).

The squared four-momentum transfer is given by

$$-t = (B-X)^2 = (A-A')^2$$ (A2)

where the particle symbols also represent their four-momenta.

The requirement of coherent reaction implies that the momentum transfer will be small, and hence also that the nucleus will have a small recoil momentum in the laboratory system. The nucleus can therefore be treated in the non-relativistic limit, and t is given by the target recoil momentum $p_{A'}$:

$$-t \simeq p_{A'}^2 = p_\perp^2 + p_\parallel^2$$ (A3)

The reaction (A1) is kinematically possible only if $m_X \gg m_B$ (i.e. $M \gg m$). This lower bound implies that, even in the exact forward direction, there is a minimum longitudinal momentum transfer Q, such that $Q^2 = t_{min}$, and

$$-t \simeq p_{A'}^2 = p^2 + Q^2$$ (A4)

Assuming the beam particle momentum $p_B = p$ to be large, one finds that

$$q \simeq p_{\perp} \quad , \quad Q \simeq \frac{M^2 - m^2}{2p} \qquad . \tag{A5}$$

Finally, we introduce the notation we will use throughout for the decomposition, into longitudinal and transverse variables, of high energies coherent processes kinematics.

Longitudinal coordinates:

z   Beam axis.

Q   Minimal longitudinal momentum transfer.

Transverse coordinates:

$\vec{b}$ Impact parameter vector.

$\vec{q}$ Transverse momentum vector.

Thus, the phase of a propagating state will be written as

$$\exp i \left(Qz + \vec{b} \, \vec{q} \right) \tag{A6}$$

A.2. Standard Glauber model[3]

In the high-energy and small momentum transfer limit, a scattering amplitude in the forward direction $f(\vec{q})$ can be connected to a so-called <u>profile function</u> $\Gamma(\vec{b})$:

$$f(\vec{q}) = \frac{ip}{2\pi} \int d^2b \, \exp\left(i \vec{q} \vec{b} \right) \Gamma(\vec{b}) \tag{A7}$$

or

$$\Gamma(\vec{b}) = \frac{1}{2\pi i p} \int d^2q \, \exp\left(-i \vec{q} \vec{b} \right) f(\vec{q}) \tag{A8}$$

The two-dimensional Fourier transforms extend over the impact parameter plane $(\vec{b})$, or the momentum transfer plane $(\vec{q})$. The Glauber model[3] expresses the profile function of a nucleus $\Gamma_A(\vec{b})$ in terms of the elementary profile functions $\Gamma_j(\vec{s}_j)$ of its nucleons by:

$$\Gamma_A(\vec{b}) = 1 - \prod_{j=1}^{A} \left[1 - \Gamma_j\left(\vec{b} - \vec{s}_j\right) \right] \tag{A9}$$

According to (A7) the <u>scattering amplitude of the nucleus</u> is then

$$F_A = \frac{ip}{2\pi} \int d^2b \; \exp\left(i\vec{q}\vec{b}\right) \; \Xi_A(\vec{b}) \tag{A10}$$

where

$$\Xi_A = \langle f | \Gamma_A | i \rangle \tag{A11}$$

is the <u>nuclear averaged profile function</u>. In an independent particle model of the nucleus, one calculates this average by taking the same nuclear density distribution $\rho(\vec{r})$ for all the nucleons. Then

$$\langle f | \cdots | i \rangle = \prod_{j=1}^{A} \int d^3r_j \; \cdots \; \rho(\vec{r}_j) \tag{A12}$$

implies

$$\Xi_A(\vec{b}) = 1 - \prod_{j=1}^{A} \left[1 - \Xi_j(\vec{b}) \right] \tag{A13}$$

where

$$\Xi_j(\vec{b}) = \int d^3r \, \rho(\vec{r}) \, \Gamma_j\left(\vec{b} - \vec{s}_j\right) \tag{A14}$$

Assuming the usual parametrization of the elastic scattering amplitude,

$$f(q^2) = \frac{(i + \alpha)}{4\pi} \, p\sigma \, \exp\left(-\beta q^2 / 2\right) \tag{A15}$$

and a spherically symmetric nuclear density normalized such that $\int d^3r \, \rho(\vec{r}) = 1$,

the averaged profile function of a nucleus becomes

$$\Xi_j(b) = (1 - ia)\sigma \int_0^\infty dq\, J_0(qb)\, e^{-\beta q^2/2} \int_0^\infty dr\, r\rho(r) \sin(qr) \quad \text{(A16)}$$

In a given nucleus one has to evaluate this profile function on protons, $\Xi_p(\sigma_p, \alpha_p, \beta_p)$ and on neutrons, $\Xi_n(\sigma_n, \alpha_n, \beta_n)$ so that the forward scattering amplitude on the nucleus is finally

$$F_A(0) = \frac{ip}{2\pi} \int d^2b \left\{ 1 - [1 - \Xi_p]^Z [1 - \Xi_n]^N \right\} \quad \text{(A17)}$$

A.3. Inelastic intermediate states.

Considering a single species of nucleons, i.e. neglecting differences between protons and neutrons, the Glauber assumption (A9) can be written

$$\Gamma_A(\vec{b}) = \sum_{j=1}^A (-1)^{j+1} \binom{A}{j} \Gamma(\vec{b})^j \quad \text{(A18)}$$

In this series, each term corresponds to the interaction of the projectile with a subset of j nucleons. In the case of elastic scattering, for all the $\binom{A}{j}$ such subsets, there is only one possible contribution, whereas for inelastic scattering there are $j!$ possible diagrams. The inelastic profile function is therefore

$$\Gamma_A^*(\vec{b}) = \sum_{j=1}^A (-1)^{j+1} \binom{A}{j} \sum_{\{j!\}} \prod_{k=1}^j \Gamma_k^*(\vec{b}) \quad \text{(A19)}$$

where the second sum is over all possible multiple scattering chains allowing for inelastic interactions. In practice one needs drastic simplifying assumptions in order to make calculations possible. As we are interested in inelastic interactions returning the projectile to its initial state, we shall assume the the dominant diagram is the one where the projectile, excited through Γ^*, rescatters like an unexcited projectile with Γ, and is returning through $\overline{\Gamma}^*$ into its initial state:

$$\Gamma_A^{*}(\vec{b}) = \sum_{j=1}^{A} (-1)^{j+1} \binom{A}{j} \sum \Gamma^{j-2} \Gamma^{*} \bar{\Gamma}^{*} \qquad (A20)$$

They are $\binom{j}{2}$ such inelastic rescattering processes possible; assuming all of them to be equivalent, we have finally

$$\Gamma_A^{*}(\vec{b}) = \Gamma^{*} \bar{\Gamma}^{*} \sum_{j=1}^{A} (-1)^{j+1} \binom{A}{j} \binom{j}{2} \Gamma^{j-2} \qquad (A21)$$

Rearangeing the combinatorial factors this can be written as

$$\Gamma_A^{*}(\vec{b}) = \frac{A(A-1)}{2} \left[1 - \Gamma(\vec{b}) \right]^{A-2} \Gamma^{*}(\vec{b}) \bar{\Gamma}^{*}(\vec{b}) \qquad (A22)$$

In deriving (A22) from (A19) we have implicitly hidden the "z ordering" complications arising from the extra phase shift introduced by the minimum longitudinal transfer Q involved in the inelastic process. From (A5) Q is

$$Q = \frac{M^2 - m^2}{2p} , \qquad (A23)$$

where M is the mass of the excited state of the projectile of initial mass m and momentum p. Because of this longitudinal momentum transfer, the profile function of an inelastic state propagating along z reads:

$$\Gamma^{*}(\vec{b}) = e^{i Q \Delta z} \frac{1}{2\pi i p} \int d^2q \, e^{-i \vec{q} \vec{b}} f^{*}(\vec{q}) \qquad (A24)$$

Then, calculating the nuclear averaged profile function $< |\Gamma_A^{*}| >$ on (A19), one gets j-fold integrations of the type[24]

$$\int_{-\infty}^{+\infty} dz_1 \, e^{i Q_{12}(z_1 - z_2)} \rho(z_1) \int_{z_1}^{+\infty} dz_2 \, e^{i Q_{23}(z_2 - z_3)} \rho(z_2) \int_{z_2}^{+\infty} \cdots \qquad (A25)$$

To avoid these integrations, we shall again assume the equivalence of all the diagrams containing pairs of excitation/desexcitation and assume identical rescattering properties for the excited and ground state of the projectile and write

$$\boxdot^{*}(\vec{b}) = A(A-1) \left[1 - \boxdot(\vec{b}) \right]^{A-2} < | \Gamma^{*}(z_1) \bar{\Gamma}^{*}(z_2) | > \qquad (A26)$$

In this expression the longitudinal integrations are understood with the constraint $z_2 > z_1$. With the usual parametrization of the inelastic amplitudes

$$f^*(t) = f^*(t=0) \, exp\left(\frac{\gamma}{2} t\right) \, , \quad \bar{f}^*(t) = \bar{f}^*(t=0) \, exp\left(\frac{\gamma}{2} t\right) \quad \text{(A27)}$$

one finds explicitely as $t = -q^2 - Q^2$

$$\boxdot_A^* = -A(A-1)\left[1 - \boxdot\right]^{A-2} \left(\frac{2\pi}{p}\right)^2 f^* \bar{f}^* \, \overline{\Phi}(Q,b) \quad \text{(A28)}$$

with

$$\overline{\Phi}(Q,b) = \int_{-\infty}^{+\infty} dz_1 \, e^{iQz_1} \, \psi(z_1) \int_{z_1}^{+\infty} e^{-iQz_2} \, \psi(z_2) \quad \text{(A29)}$$

and

$$\psi(z) = \frac{1}{\gamma} \int_0^{\infty} dr \, r \, I_0\left(\frac{br}{\gamma}\right) \bigg/ \left(\sqrt{r^2 + z^2}\right) exp\left(-\frac{r^2 + b^2}{2\gamma} - \frac{Q^2 \gamma}{2}\right) \quad \text{(A30)}$$

For diffractively produced inelastic intermediate states, the amplitudes f^* and $\bar{f}^*$ are complex conjugated. Therefore (Kaidalov, Kondratyuk[20]):

$$f^*(0) \, \bar{f}^*(0) \frac{\pi}{p^2} = \frac{d\sigma}{dt}(t=0) = \int dM^2 \frac{d^2\sigma}{dt \, dM^2} \quad \text{(A31)}$$

Inserting this into (A28) the nuclear averaged profile function becomes

$$\boxdot_A^* = -4\pi A(A-1)\left[1 - \boxdot\right]^{A-2} \int dM^2 \frac{d^2\sigma}{dt \, dM^2} \, \overline{\Phi}(Q,b) \quad \text{(A32)}$$

The calculation of the inelastic rescattering form factor $\overline{\Phi}(Q,b)$ can be carried out analytically in the case of a gaussian nuclear density

$$\rho(r) = \left(\pi G^2\right)^{-3/2} exp\left(-r^2 / G^2\right) \, , \quad \text{(A33)}$$

yielding

$$\overline{\Phi}(Q,b) = \frac{1}{2\left(2\pi z^2\right)^2} \, exp\left(-b^2/z^2 - Q^2 z^2\right)\left[1 - erf(iQz)\right] \, , \quad \text{(A34)}$$

where

$$x^2 = \frac{1}{2}\left(G^2 + 2\gamma\right) \tag{A35}$$

In this form factor, the complex error function araises because of the z-ordering (Ikeda[25], Trefil[26]). This extra phase produces anti-shadowing at low momenta in heavy nuclei. Although the gaussian approximation (A23) is known to be correct only at the 10 % level for heavy nuclei, we shall use it for the inelastic form factor because the integrations (A29,A30) are numerically quite time consuming. Finally, with (A10), the correction to the scattering amplitude (A17) due to the inelastic intermediate states is

$$F_A^*(0) = -2ip\,A(A-1)\int d^2b\,\left[1 - \Xi\right]^{A-2}\int dm^2\,\frac{d\sigma(0)}{dt\,dm^2}\,\bar{\Phi}(Q,b) \tag{A36}$$

In practical calculations we shall take for the elastic profile function Ξ an average defined as

$$\left(1 - \Xi\right)^A \equiv \left(1 - \Xi_p\right)^Z \left(1 - \Xi_n\right)^N \tag{A37}$$

Formula (A36) expresses the inelastic shadow correction in terms of nuclear form factors and the inclusive diffraction dissociation cross-section of the projectile on nucleons :

$$K + N \longrightarrow X + N \tag{A38}$$

A.4. The Karmanov-Kondratyuk formula

Let us see under which assumptions our result (A36) can be simplified in the case of the inelastic shadow correction to the total cross-section

$$\Delta\sigma_T = 2\int d^2b\,\Xi_A^*(b) \tag{A39}$$

If one neglects the q^2 dependence in the inelastic form factor, therfore

taking the limit $\gamma \to 0$ in (A30), one sees that $\varphi(z) \simeq \rho(\sqrt{b^2 + z^2})$. Neglecting the z-ordering as well, (A29) then becomes

$$\bar{\Phi}(Q,b) \simeq \frac{1}{2}\left[\int_{-\infty}^{+\infty} dz \, e^{iQz} \rho(\sqrt{b^2 + z^2})\right]^2 \qquad (A40)$$

Similarely, in the limit $\beta \to 0$, $\alpha \to 0$ the elastic profile function (A16) simplifies to

$$\Xi(b) \simeq \frac{1}{2}\sigma \int_{-\infty}^{+\infty} dz \, \rho(\sqrt{b^2 + z^2}) \equiv \frac{1}{2}\sigma T(b) \qquad (A41)$$

Finally, taking the limit $A \to \infty$, the power series in (A36) can be replaced by an exponential giving

$$\Delta\sigma_T \simeq -4\pi A^2 \int d^2b \, \exp\left[-\frac{A}{2}\sigma T(b)\right] \int dM^2 \frac{d^2\sigma(0)}{dt \, dM^2} \bar{\Phi}(Q,b) \quad (A42)$$

This is with (A40,A41) the Karmanov-Kondratyuk result[4].

A.5. Deuterium case, Pumplin-Ross formula, Gribov formula.

Setting A=2 in (A36) we obtain

$$F^{*} = -4i\rho \int d^2b \int dM^2 \frac{d^2\sigma(0)}{dt \, dM^2} \underline{\Phi}(Q,b) \qquad (A43)$$

performing the impact parameter integration we find

$$F^{*} = \frac{-i\rho}{\pi(\sigma^2 + 2\gamma)} \int dM^2 \frac{d^2\sigma(0)}{dt \, dM^2} \exp\left[-Q^2(\sigma^2 + 2\gamma)/2\right]\left[1 - \text{erf}\left(\frac{iQ\sigma}{\sqrt{2}}\right)\right] (A44)$$

This the Pumplin-Ross formula[27] which gives, via the optical theorem, the following correction to the hadron-deuteron total cross-section

$$\Delta\sigma_T = \frac{-4}{\sigma^2 + 2\gamma} \int dM^2 \frac{d^2\sigma(0)}{dt \, dM^2} \exp\left[-Q^2(\sigma^2 + 2\gamma)/2\right] \qquad (A45)$$

This result can be obtained starting from the classical Gribov formula[28]

$$\Delta \sigma_T = -2 \int dq^2 \int dM^2 \frac{d^2\sigma(t)}{dt\,dM^2}\,S(t) \qquad \text{(A46)}$$

with the diffractive dissociation parametrized as

$$\frac{d^2\sigma}{dt\,dM^2}(t) = \frac{d^2\sigma(0)}{dt\,dM^2}\,\exp(\gamma t) \qquad \text{(A47)}$$

and the deuterium form factor written as

$$S(t) = \exp(t\,G/2) \qquad \text{(A48)}$$

where

$$-t = q^2 + Q^2 \qquad \text{(A49)}$$

B. REGGE MODEL OF THE FORWARD SCATTERING AMPLITUDE

B.1. Regge poles

For high-energy small-angle scattering, a single Regge-pole contribution to a s-channel amplitude $A = A(a+b \rightarrow c+d)$ is an expression like[7]

$$B(s,t) = \frac{\gamma(t)}{4\pi}\left[i + \tau\left(\tan\frac{\pi}{2}\alpha(t)\right)^\tau\right]\left(\frac{\nu}{\nu_0}\right)^{\alpha(t)} \tag{B1}$$

where

$$\nu = \frac{1}{2}(s-u) \tag{B2}$$

ν_0 is a scale factor ($\nu_0 = 1 \text{ GeV}^2$) and $\tau = \pm 1$ is the signature. Thus the total amplitude will be

$$A(s,t) = \sum_j B_j(s,t) \tag{B3}$$

where the sum extends over the trajectories that can be exchanged.

In the laboratory system, with $p_b = p$ the beam momentum, one has

$$\nu = \frac{1}{2}(s-u) = m_a\sqrt{m^2_b + p^2} \tag{B4}$$

and the optical theorem reads

$$\sigma_T = \frac{4\pi}{p} \text{Im } A(s, t=0) \tag{B5}$$

It is convenient for the fits to introduce the notation

$$S^\tau = \frac{4\pi}{p} B(\alpha, \gamma, \tau; s, t) \tag{B6}$$

such that the imaginary part of

$$S(s,t) = \sum_j S_j^{\tau}$$
(B7)

which corresponds to (B3), gives directely the total cross-section.

The basic formula of the Regge theory, (A1), provides an explicit separation of the t dependence from the s, u dependence. It turns out phenomenologically, for our purpose of parametrizing the amplitude near t=0, that such a separation is also possible for (B7). One finds

$$S(s,t) = \exp\left(-\frac{\beta}{2}|t| + \frac{S}{2}t^2\right) \sum_j S_j^{\tau}(s, t=0)$$
(B8)

where one thus neglects the individual t dependences of the trajectories (α'_j) and of the residues (γ'_{0j}), but one leaves a common t dependence factor describing the forward elastic scattering peak.

B.2. Imaginary part of the forward amplitude

We now concentrate on the total cross-section parametrization. Let us denote the diffractive component of the total cross-section, i.e. the Pomeron, by D(ab). The Regge phenomenology gives:

$$s(K^-p) = D(K^-p) + S_f^- + S_\rho^+ + S_\omega^+ + S_{A_2}^-$$

$$s(K^+p) = D(K^+p) + S_f^- - S_\rho^+ - S_\omega^+ + S_{A_2}^-$$
(B9)

$$s(K^-n) = D(K^-n) + S_f^- - S_\rho^+ + S_\omega^+ - S_{A_2}^-$$

$$s(K^+n) = D(K^+n) + S_f^- + S_\rho^+ - S_\omega^+ - S_{A_2}^-$$

The same formulae hold for proton-nucleon scattering, provided one substitutes p for K^+ and $\bar{p}$ for K^-. For pion-nucleon scattering, the corresponding formulae are

$$S(\pi^- p) = S(\pi^+ n) = D(\pi N) + S_f^- + S_\rho^+$$

$$S(\pi^- n) = S(\pi^+ p) = D(\pi N) + S_f^- - S_\rho^+ \qquad \text{(B10)}$$

Of course, while the intercepts of the Regge trajectories are expected to be the same for all three families of incident beam particles, their respective residues are different. Nevertheless, this equality of their intercepts will help us in fitting unambiguously(B9) and (B10) to the data, a task that would otherwise be difficult because of the number of free parameters. To reduce the number of free parameters, we will furthermore assume strong exchange degeneracy, which is the assertion

$$\left.\begin{array}{l} \alpha_\omega = \alpha_f \\[2mm] \gamma_\omega = \gamma_f \end{array}\right\} \qquad\qquad \left.\begin{array}{l} \alpha_\rho = \alpha_{A_2} \\[2mm] \gamma_\rho = \gamma_{A_2} \end{array}\right\} \qquad \text{(B11)}$$

This strong exchange degeneracy hypothesis (which results theoretically from the absence of u-channel, or "exchange" forces) implies that the $(K^+ N)$ and $(p N)$ total cross-sections depend only on the diffractive term. Explicitely

$$\sigma_T(K^- p) = \operatorname{Im} D(K^- p) + \frac{2}{p}\left(\gamma_\omega \nu^{\alpha_\omega} + \gamma_\rho \nu^{\alpha_\rho}\right)$$

$$\sigma_T(K^+ p) = \operatorname{Im} D(K^+ p)$$

$$\sigma_T(K^- n) = \operatorname{Im} D(K^- n) + \frac{2}{p}\left(\gamma_\omega \nu^{\alpha_\omega} - \gamma_\rho \nu^{\alpha_\rho}\right) \qquad \text{(B12)}$$

$$\sigma_T(K^+ n) = \operatorname{Im} D(K^+ n)$$

In this model, the only contribution to $\sigma_T(K^+ n)$ and $\sigma_T(K^+ p)$ are from the Pomeron. In order to accommodate the observed difference in these two cross-sections, we will allow the Pomeron contribution to be different for proton and neutron targets. In agreement with the Pomeranchuk theorem

(stating the equality of total cross-sections of particles and anti-particles on the same target at infinite momentum) we set therefore

$$D(K^-p) = D(K^+p) \equiv D(Kp)$$

$$D(K^-n) = D(K^+n) \equiv D(Kn) \tag{B13}$$

Clearly, this distinction between D(Kp) and D(Kn) cannot be given too much physical content, as it will "buffer" experimental errors as well as possible exchange degeneracy breaking.

For the Pomeron we take a Froissart like behaviour of its momentum dependence. This parametrization of the diffraction term is currently favored by many phenomenologists[29] and has recently received theoretical support from parton models[30]. We shall write

$$\text{Im } D(Kp) = a_p + b_p \log^2 (p/c_p)$$

$$\text{Im } D(Kn) = a_n + b_n \log^2 (p/c_n) \tag{B14}$$

B.3. Real part of the forward amplitude

The real part of the Regge-pole contribution is directly given by (A1), it thus remains to find the real part corresponding to the diffractive term (B14). This real part could be directly obtained from analyticity and crossing properties in the asymptotic region. But, in order to obtain a precise prediction for the real part in the intermediate region already, we shall express it by the dispersion relation

$$\text{Re } D(KN) = \frac{2}{\pi} p \int_{p_0}^{\infty} dx \frac{\text{Im } D(KN)}{x^2 - p^2} \tag{B15}$$

And, in this relation, the threshold p_0 will be adjusted in each channel

to give good agreement of the real parts at 5 GeV/c with the recent disper-
sion relation calculations of Jenni et al.[31]. This prescription insures that
resonance and threshold effects, which have logarithmic terms affecting the
intermediate energy region, are properly taken care of.

B.4. Fitting and results

In our approach the real parts are essentially predicted from the imaginary
parts. The fitting procedure consists thus primarily in adjusting (B12, B13,
B14) to the total cross-section data[32].

As it is well known, the kaon-nucleon and proton-nucleon total cross-section
differences are dominated by the ω-trajectory. It is thus easy to extract
the omega contribution and one finds $\alpha_\omega(0)=0.44\pm0.01$ for kaons and $\alpha_\omega(0)=$
0.44±0.02 for protons, in excellent agreement. From (B10) one sees that
the pion-nucleon total cross-section difference is dominated by ρ exchange.
Fitting the pion data one gets $\alpha_\rho(0)=0.57\pm0.01$. The $\alpha_\rho(0)$ obtained by
fitting kaons to (B12) gives $\alpha_\rho(0)=0.55\pm0.03$ and is thus in good agreement
with the pion induced intercept. On the other hand, the ρ contribution to
the proton-nucleon scattering is too small to give relevant results in an
unconstrained fit. So the ρ intercept $\alpha_\rho(0)=0.12\pm0.28$ found by fitting (B12)
to the proton data is meaning less.

Having adjusted the thresholds in (B15) to give reasonable real parts in
the low energy region, one is in position to check the quality of these fits
by using them to predict cross-sections for charge-exchange reactions and
regeneration in hydrogen. One has :

$$\frac{d\sigma}{dt}\left(K^+n\to K^0p\right)=\frac{1}{16\pi}\left|S(K^+p)-S(K^+n)\right|^2 \tag{B16}$$

$$\frac{d\sigma}{dt}\left(K^-p\to \bar{K}^0n\right)=\frac{1}{16\pi}\left|S(K^-p)-S(K^-n)\right|^2 \tag{B17}$$

$$\left|\frac{f-\bar{f}}{p}\right|\left(K_Lp\to K_Sn\right)=\frac{1}{4\pi}\left|S(K^+n)-S(K^-n)\right| \tag{B18}$$

These three predictions are tabulated in Table 8.3 together with the fitted total cross-sections and calculated real parts for the four kaon-nucleon channels. In Fig. B.1 and Fig B.2 we compare charge-exchange and regeneration in hydrogen with the data. Considering that these three predictions are based on small differences of the fitted amplitudes depending on both the imaginary and real parts of the fitted amplitudes, the agreement with the data (above the resonnance region) is excellent. Especially the agreement with the preliminary results of regeneration by H at FNAL energies[14] is a strong indication of the correctness of the omega intercept, i.e. $\alpha_\omega(0)=0.44\pm0.01$.

The internal consistency found by us in the Regge fits to the kaon-nucleon system strongly suggests that the value of $\alpha_\omega(0)$ derived from regeneration from carbon[5], (i.e. $\alpha_\omega(0)=0.397\pm0.003$, after correction for $|\eta_{+-}|=2.183$ x 10^{-3}) is not the "true" ω intercept, but rather an intercept modified by "nuclear effects". To see what the "carbon intercept" would imply for regeneration in hydrogen, we have drawn in Fig. B.2 the prediction obtained by constraining the total cross-section fits to $\alpha_\omega(0)=0.40$. The difference is over 50% in the modulus and over 15° in the phase at 100 GeV/c, in clear disagreement with the data.

In Table 8.2 we give the parameters resulting from the fits in the four following cases :

(i)   Normal fit yielding $\alpha_\omega(0)=0.44\pm0.01$ and $\alpha_\rho(0)=0.55\pm0.02$.

(ii)   Constrained fit with $\alpha_\rho(0)=0.57$.

(iii) Constrained fit with $\alpha_\rho(0)=0.57$ and $\alpha_\omega(0)=0.40$.

(iv)   Constrained fit with $\alpha_\omega(0)=0.40$.

B.5. Forward elastic peak parametrization

We take for the elastic scattering parameters defined in (B8) the results of an "eye-ball" fit to the data compiled in[33]. This procedure is precise enough (i.e. ±10%) for our purpose. We find

$$\beta(p) = 6.5 + .81 \, \log(s) \qquad S(p) = 1.9 \qquad \text{(B19)}$$

$$\beta(\bar{p}) = 11.5 + .16 \, \log(s) \qquad S(\bar{p}) = 3.0 \qquad \text{(B20)}$$

$$\beta(\pi^+) = 6.5 + .49 \, \log(s) \qquad \delta(\pi^+) = 2.1 \qquad \text{(B21)}$$

$$\beta(\pi^-) = 8.0 + .22 \, \log(s) \qquad \delta(\pi^-) = 2.7 \qquad \text{(B22)}$$

$$\beta(K^+) = 2.0 + 1.2 \, \log(s) \qquad \delta(K^+) = 2.0 \qquad \text{(B23)}$$

$$\beta(K^-) = 7.0 + .38 \, \log(s) \qquad S(K^-) = 2.5 \qquad \text{(B24)}$$

ACKNOWLEDGMENTS

REFERENCES

1. See, for example, J. Steinberger, "K^O Decay and CP violation", CERN 70-1.

2. P.V.R. Murthy et al., Nucl. Phys., B92(1975)269.

3. R.J. Glauber, Phys. Rev. 100(1955)242;
   V. Franco and R.J. Glauber, Phys. Rev. 142(1966)1195.

4. V. Karmanov and L. Kondratyuk, ZhETF Pisma 18(1973)451;
   JETP Letters (Sov.Phys.) 18(1973)266.

5. J. Roehrig et al., Phys. Rev. Lett. 38(1977)1116;
   J. Roehrig, PhD thesis, University of Chicago, (1977).

6. R.E. Hendrick et al., Phys. Rev. D11(1975)536;
   A. Bouquet and B. Diu, Preprint PAR/LPTHE 75/9, (1975).

7. P.D.B. Collins, "An introduction to Regge theory and high energy physics",
   Cambridge University Press, (1977).

8. LAM Grader, CERN Specs 064, (1972).

9. EFI Electronics Shop, University of Chicago.

10. Particle Data Group, Rev. Mod. Phys. 48(1976).

11. G. Jarlskog and L. Jönsson, CERN computer center program library, W601.

12. V.L. Highland, Nucl. Instr. and Meth. 129(1975)497. See also [10].

13. D. Luers et al. Phys. Rev. 133(1964)B1276.

14. G. Bock et al., Preliminary results from Fermilab experiment 425 (K$_S$
    Regeneration from Hydrogen), to be published.

15. R. Devoe, PhD thesis, University of Chicago (1977). See also [5,51,54].

16. M.L. Good, Phys. Rev. 106(1957)591.

17. E.S. Abers et al., Nuovo Cimento 42A(1965)365. See also [27,28].

18. O.V. Kancheli, ZhETF Pis. Red. 18(1973)465;
    J. Koplik and A.H. Mueller, Phys. Rev. D12(1975)3638.

19. Y. Akimov et al., Fermilab-Pub-77/88-EXP(1977). Submitted to Phys. Rev. Lett.

20. A.B. Kaidalov and L.A. Kondratyuk, Nucl. Phys B56(1973)90;
    A.B. Kaidalov and L.A. Kondratyuk, ZhETF Pis. Red. 15(1972)170.

21. V. Franco, Phys. Rev. C6(1972)748.

22. G. Feinberg, Phys. Rev. 109(1958)1381.

23. N.M. Kroll, T.D. Lee and B. Zumino, Phys. Rev. B98(1975)215.

24. L. Bertocchi, Nuovo Cimento 11A(1972)45.

25. M. Ikeda, Phys. Rev. C6(1972)1608.

26. J.S. Trefil, Phys. Rev. D3(1971)1615.

27. J. Pumplin and M. Ross, Phys. Rev. Lett. 21(1968)1778.

28. V. N. Gribov, Sov. Phys. JETP 29(1969)483.

29. R.G. Roberts et al., RL-77-088/A (1977). See also [6].

30. E.M. Levin and M.G. Ryskin, LIYF 370, Leningrad, (1977).

31. M. Ferro-Luzzi and P. Jenni, CERN/EP/PHYS 77-55, (1977). Submitted to Nuclear Physics B.

32. E. Bracci et al., CERN/HERA 72-2, Compilation, (1972);
    A.S. Carroll et al., Phys. Lett. 61B(1976)303.

33. D.S. Ayres et al., Phys. Rev. D15(1977)3105.

34. W.R. Molzon et al., Preliminary results from Fermilab experiment 226 (K^o elecro-magnetic formfactor measurement), to be published.

35. A.B. Kaidalov and V.A. Khoze, LIYF 193, Leningrad, (1975).

36. S. Shlomo and E. Friedman, Phys. Rev. Lett. 39(1977)1180.

37. G.D. Alkhazov et al., Phys. Lett. 57B(1975)47. See also
    B. Zeidman et al., Phys. Rev. Lett 40(1978)1316.

38. C.W. DeJager et al., At. Data Nucl. Data Tables 14(1974)479.

39. A.Y. Abul-Magd, Nucl. Phys. B8(1968)638.

40. V.L. Telegdi, Vth International conference on High-Energy Physics and Nuclear Structure, (1975), Editors D.E. Nagel et al.

41. C.A. Ayre and M.J. Longo, Phys. Lett. 62B(1976)299.

42. See [25,26].

43. Prof. B. Winstein, private communication.

44. D.R. Harrington, Phys. Lett 51B(1974)287.

45. L. Caneschi and A. Schwimmer, CERN Th-2299. To appear in the proceedings of the XII th Rencontre de Moriond-Flaine, (1977).

46. H. Foeth et al., Phys. Lett. 31B(1970)544.

47. W.L. Lankin et al. Phys. Lett. 31B(1970)677.

48. H. Sticker, PhD thesis, Nevis 205, (1974).

49. F. Dydack et al. Nucl. Phys. B102(1976)264.

50. H. Faissner et al., Phys. Lett. 30B(1969)206.

51. W.C. Carithers et al., Nucl. Phys. B118(1977)333.

52. P. Darriulat et al., Phys. Lett. 33B(1970)433.

53. G.W. Brandenburg et al., Phys. Rev. D9(1974)1939.

54. V.K. Birulev et al., Nucl. Phys. B115(1976)249.